Endocytosis against high turgor pressure is made easier by partial protein coating and a freely rotating base

Rui Ma[1,2*] **and Julien Berro**[1,2,3*]

***For correspondence:**
ruima86@gmail.com (RM);
julien.berro@yale.edu (JB)

[1]Department of Molecular Biophysics and Biochemistry, Yale University, New Haven, CT 06520, USA; [2]Nanobiology Institute, Yale University, West Haven, CT 06516, USA; [3]Department of Cell Biology, Yale University School of Medicine, New Haven, CT 06520, USA

Abstract During clathrin-mediated endocytosis, a patch of flat plasma membrane is deformed into a vesicle. In walled cells, such as plants and fungi, the turgor pressure is high and pushes the membrane against the cell wall, thus hindering membrane internalization. In this paper, we study how a patch of membrane is deformed against turgor pressure by force and by curvature-generating proteins. We show that a large amount of force is needed to merely lift the membrane up and an even larger force is needed to pull a membrane tube. The magnitude of these forces strongly depends on how the base of the membrane is constrained and how the membrane is coated with curvature-generating proteins. In particular, these forces can be reduced by partially but not fully coating the membrane patch with curvature-generating proteins. Our theoretical results show excellent agreement with experimental data.

Introduction

Clathrin-mediated endocytosis (CME) is an active process eukaryotic cells use to transport materials from their outside environment to inside of the cell (***McMahon and Boucrot, 2011***; ***Sorkin and Puthenveedu, 2013***; ***Lu et al., 2016***; ***Kaksonen and Roux, 2018***; ***Lacy et al., 2018***; ***Mettlen et al., 2018***). During CME, a patch of flat plasma membrane is bent into the cell (***Figure 1***) and severed to release a vesicle. Deforming the membrane towards the cytoplasm is opposed by membrane's resistance to bending and membrane tension (***Boulant et al., 2011***; ***Wu et al., 2017***). In walled cells such as plants and fungi, the inward deformation is also opposed by turgor pressure, which pushes the membrane against the cell wall (***Low and Chandra, 1994***; ***Aghamohammadzadeh and Ayscough, 2009***; ***Basu et al., 2014***). In yeast cells, the inner pressure can be up to $1.5\ \mathrm{MPa}$ (***Minc et al., 2009***; ***Atilgan et al., 2015***). It is believed that as a consequence of this high pressure, the membrane invagination exhibits a narrow tubular shape in yeast with a diameter of $\sim 30\ \mathrm{nm}$ (***Kukulski et al., 2012***), while in mammalian cells the invagination exhibits a spherical shape with a diameter of $\sim 100\ \mathrm{nm}$ due to a relatively low pressure ($\sim 1\mathrm{kPa}$) (***Avinoam et al., 2015***).

In the past decade several theoretical models have been proposed to account for the membrane shape evolution during CME (***Agrawal and Steigmann, 2008***; ***Walani et al., 2015***; ***Dmitrieff and Nédélec, 2015***; ***Hassinger et al., 2017***; ***Alimohamadi et al., 2018***). Most of these models have assumed conditions relevant to mammalian cells, i.e. low turgor pressure ($< 1\ \mathrm{kPa}$) and focused

on the role of membrane tension. Such tension-dominant membrane deformations have also been extensively studied in *in vitro* experiments where membrane tethers are pulled from giant liposomes (***Koster et al., 2005***; ***Cuvelier et al., 2005***; ***Dimova et al., 2006***). In contrast, the pressure-dominant regime of membrane deformations, which is relevant to endocytosis in walled cells, has been rarely studied (***Dmitrieff and Nédélec, 2015***). The typical force barrier to invaginate a membrane tube against a membrane tension of $0.01\ \mathrm{pN/nm}$ is only $10 - 100\ \mathrm{pN}$, whereas a substantial force ($\sim 3000\ \mathrm{pN}$) is required to overcome a turgor pressure of $1\ \mathrm{MPa}$ (***Carlsson, 2018***; ***Lacy et al., 2018***).

The cytoskeleton protein actin is essential for generating the forces required for CME in yeast cells (***Kübler and Riezman, 1993***; ***Engqvist-Goldstein and Drubin, 2003***; ***Yarar et al., 2005***; ***Sun et al., 2006***; ***Kaksonen et al., 2006***; ***Aghamohammadzadeh and Ayscough, 2009***; ***Mooren et al., 2012***; ***Goode et al., 2015***). However, the exact organization of actin filaments around the membrane invagination remains elusive. Actin filaments are likely organized into a tight meshwork since ribosomes are excluded from endocytic sites (***Figure 1***a) and actin filaments are heavily crosslinked (***Berro and Pollard, 2014***). How the actin machinery produces force to bend the membrane remains unclear. The most commonly accepted hypothesis is that polymerization of actin filaments is converted into a pulling force acting on the tip of the invagination through a push-pull mechanism (***Carlsson and Bayly, 2014***; ***Wang et al., 2016***; ***Tweten et al., 2017***; ***Mund et al., 2018***). In this mechanism, actin filaments are nucleated on a ring around a patch of clathrin and adaptor proteins that link the tip of the invagination to the actin meshwork. Polymerization of actin filaments at the base of the invagination pushes the actin meshwork away from the plasma membrane, and in turn pulls the invagination inwards thanks to the adptor proteins that link actin filaments to the membrane.

Membrane can also be bent by proteins that induce membrane curvature. Clathrin molecules can assemble into a cage-like icosahedral lattice composed of hexagons and pentagons *in vitro* (***Kirchhausen and Harrison, 1981***; ***Fotin et al., 2004***). The clathrin-lattice alone is able to induce spherical buds from membrane in reconstituted experiments (***Dannhauser and Ungewickell, 2012***). In yeast cells, the clathrin lattice acts as a scaffold linked to the plasma membrane via adaptor proteins and they together form a rigid coat at the membrane invagination tip (***Jin et al., 2006***; ***Lherbette et al., 2019***). Based on measurements of the copy number of clathrin molecules in yeast cells, this coat is expected to form a hemi-spherical cap (***Sirotkin et al., 2010***). Many clathrin-associated proteins, such as BAR-domain proteins and epsin, have also shown the capacity to induce membrane curvature and might help with CME (***Gallop et al., 2006***; ***Henne et al., 2007***).

In this paper, we study CME under conditions of high turgor pressure and low membrane tension by investigating a theoretical model, which describes how a membrane patch is deformed by a point force and by proteins that induce membrane curvature. In the absence of coat proteins, we show that as a result of high turgor pressure ($1\ \mathrm{MPa}$), a large amount of force ($\sim 300\ \mathrm{pN}$) is needed to merely lift up the membrane and an even larger force ($\sim 3000\ \mathrm{pN}$) is needed to pull a membrane tube. This is very different from pulling a tube against low turgor pressure, like in mammalian cells, where a small amount of force ($\sim 10\ \mathrm{pN}$) is able to pull a membrane tube (***Hassinger et al., 2017***).

We also show that the constraints at the base of the membrane patch have a dramatic effect on the force requirements to lift up the membrane patch and pull a membrane tube. In particular, we show that whether the angle at the base can freely rotate makes a qualitative difference on whether the membrane can be spontaneously lifted up without any forces.

We show that the forces to deform membranes that are partially coated with curvature-generating proteins and membranes that are fully-coated have qualitatively and quantitatively different profiles. By partially coating the membrane, the force barrier that is usually present for fully-coated membranes can be dramatically reduced to zero, which implies that the membrane can be spontaneously curved up into a vesicular shape.

We find excellent agreement between our theory and experiments. With a single set of parameters for the partially coated membrane model, we can fit geometric features of the membrane

shape obtained via electron tomography across different stages of CME. From the comparison, we estimate that the force required for CME in yeast cells is $\sim 2000\,\mathrm{pN}$ if the membrane angle at the base is free to rotate.

Results

Model of the membrane at the endocytic site

We model the membrane at the endocytic site as an axisymmetric two-dimensional surface. The shape of the membrane is parameterized with its meridional coordinates $(R(s), Z(s))$, where s is the arclength along the meridional direction (***Figure 1***c). The angle $\psi(s)$ spans between the tangential direction and the horizontal direction. The actin polymerization force is modeled as a point force f acting at the symmetric center of the membrane, which is lifted to a height L relative to the cell wall (***Figure 1***c). The membrane patch is in contact with the cell wall at a base radius of R_b. Outside of R_b there is a lipid reservoir such that the membrane tension σ is kept constant at the base points. An isotropic turgor pressure p is exerted on the membrane, which possesses a bending rigidity κ and spontaneous curvature c_0 due to protein coating. The free energy of the membrane, which takes into account of the influence of curvature-generating proteins, can be written as

$$F = \frac{\kappa}{2}\int (2H - c_0)^2\,\mathrm{d}A + \sigma A + pV - fL, \tag{1}$$

where H denotes the mean curvature of the membrane surface (***Helfrich, 1973***), A denotes the surface area and V denotes the volume between the membrane and the cell wall. We consider both a homogeneous model where the spontaneous curvature c_0 is spatially uniform - such as a bare membrane or a membrane fully coated with curvature-generating proteins - and an inhomogeneous model where c_0 is spatially varied - such as a membrane partially coated by curvature-generating proteins.

Due to rotational symmetry about the z-axis, the free energy of the membrane in ***Equation 1*** can be expressed as a functional

$$F = 2\pi\int_0^S \mathcal{F}[\psi, R, \dot{\psi}, \dot{R}, \gamma]ds, \tag{2}$$

where $\dot{\psi}$ and $\dot{R}$ denote their derivatives with respect to the arclength s, S denotes the total arclength from the tip to the base, γ is a Lagrangian multiplier that enforces the geometric relation $\dot{R} = \cos\psi$ (see Derivation of the membrane shape equations). The shape of the membrane is determined by minimization of the free energy F with proper boundary conditions (BCs) at the base. Small variations of $\delta\psi$ and δR result in variation of the free energy δF, which consists of boundary terms like $\frac{\partial\mathcal{F}}{\partial\dot{\psi}}\delta\psi$ and $\frac{\partial\mathcal{F}}{\partial\dot{R}}\delta R$. Four types of BCs at the base can be identified by letting these boundary terms vanish (***Table 1***). Physically they correspond to the combination of whether the base radius is fixed or variable, and whether the angle of the membrane at the base is fixed (parallel to the cell wall) or free to rotate. We focus on the two BCs where the base radius is fixed ($R = R_\mathrm{b}$) and refer them as free-hinge BC (BC1 in ***Table 1***) if the membrane is free to rotate ($\frac{\partial\mathcal{F}}{\partial\dot{\psi}} = 0$) and fixed-hinge BC (BC2 in ***Table 1***) if the angle of membrane at the base is fixed to zero ($\psi = 0$). We also compare our results with a previous work ***Dmitrieff and Nédélec (2015)***, which studied a fully-coated membrane with a BC where the base is free to move and the angle of the membrane at the base is fixed (BC4 in ***Table 1***).

The characteristic forces for membrane tube elongation are different between pressure-dominant and tension-dominant conditions.

To demonstrate the distinct physics of CME between pressure-dominant and tension-dominant conditions, we approximate the elongated endocytic invagination (as in ***Figure 1***a, for example) as a cylindrical tube of radius R and length L and derive analytic formulas for the forces to elongate

Table 1. Possible boundary conditions at the base of the endocytic membrane.

	Base radius	Membrane angle at the base	Mathematical definition
BC1[a]	fixed	free	$R = R_b$, $\frac{\partial \mathcal{F}}{\partial \dot{\psi}} = 0$
BC2[b]	fixed	fixed	$R = R_b$, $\psi = 0$
BC3	free	free	$\frac{\partial \mathcal{F}}{\partial \dot{R}} = 0$, $\frac{\partial \mathcal{F}}{\partial \dot{\psi}} = 0$
BC4[c]	free	fixed	$\frac{\partial \mathcal{F}}{\partial \dot{R}} = 0$, $\psi = 0$

[a] Referred to as the free-hinge BC
[b] Referred to as the fixed-hinge BC
[c] BC4 has been studied in ***Dmitrieff and Nédélec*** (***2015***) for a fully coated membrane.

Table 2. Fitting parameters to compare with experimental data

Symbols	Physical meaning	Values for the free-hinge BC	Values for the fixed-hinge BC
p	Turgor pressure	1 MPa	1 MPa
R_p	Characteristic tube radius	15 nm	18 nm
c_0	Spontaneous curvature of the membrane induced by protein coat	0.067 nm^{-1}	0.056 nm^{-1}
a_0	Coating area of proteins	1414 nm^2	2036 nm^2
R_b	Base radius of the membrane patch	30 nm	36 nm
σ	Surface tension at the base	0.03 pN/nm	0.036 pN/nm
α	Control parameter for the sharpness of the coating edge	0.007 nm^{-2}	0.005 nm^{-2}

a membrane tube. The free energy ***Equation 1*** under this approximation becomes

$$F_{\text{tube}} = 2\pi RL\left[\frac{\kappa}{2}\left(\frac{1}{R} - c_0\right)^2 + \sigma + \frac{pR}{2}\right] - fL. \tag{3}$$

In the case of pressure-dominant condition ($\sigma = 0$ and $c_0 = 0$), by minimization of the free energy ***Equation 3*** with respect to R and L, we obtain the characteristic tube radius R_p and the corresponding force f_p (***Dmitrieff and Nédélec, 2015***):

$$R_p = \left(\frac{\kappa}{2p}\right)^{1/3} \quad , \quad f_p = 3\pi R_p^2 p = \frac{3\pi}{2}\left(2\kappa^2 p\right)^{1/3}. \tag{4}$$

Note that the tube radius scales with the turgor pressure as $R_p \propto p^{-1/3}$, but the force obeys $f_p \propto p^{1/3}$. This means a higher turgor pressure results in a narrower tube, but needs larger forces to elongate. In the case of tension-dominant condition, the characteristic tube radius R_σ and force f_σ read (***Derényi et al., 2002***):

$$R_\sigma = \left(\frac{\kappa}{2\sigma}\right)^{1/2} \quad , \quad f_\sigma = 4\pi R_\sigma \sigma = 2\pi\left(2\kappa\sigma\right)^{1/2}. \tag{5}$$

As for endocytosis in yeast cells, $\sigma \approx 0.01$ pN/nm (***Hassinger et al., 2017***), $p \approx 1$ MPa (***Minc et al., 2009***; ***Atilgan et al., 2015***) and $\kappa \approx 300 k_{\mathrm{B}}T$ (***Jin et al., 2006***). These numbers lead to a rough estimation of $R_{\mathrm{p}} \approx 8.5$ nm, $f_{\mathrm{p}} \approx 700$ pN and $R_{\sigma} \approx 250$ nm, $f_{\sigma} \approx 30$ pN. The radius of long endocytic invaginations observed experimentally is about 15 nm (***Kukulski et al., 2012***), which is much closer to the estimated R_{p} than the estimated R_{σ}, thus supporting the idea that turgor pressure but not membrane tension is the dominant factor that opposes endocytosis in yeast cells.

A large base radius lowers the force barrier to pull a membrane tube against turgor pressure.

We first consider the case of a membrane at the endocytic site void of any curvature-generating proteins (i.e., $c_0 R_{\mathrm{p}} = 0$), and study the effect of base radius on the required forces to pull a membrane tube. The effect of forces on the membrane deformation is characterized by the force-height (f-L) curve, which in general is non-monotonic (***Figure 2***a - d). A force barrier $F_{\max}$ appears at a relatively low height L when the membrane is dome-shaped (***Figure 2***a - d, inset, labeled by circles). As the membrane is lifted further up, the membrane changes from a dome-shape to an Ω-shape, when a narrow neck appears (signaled by the tangential angle $\psi = \pi/2$ at an intermediate arclength). The force f then decreases with L and approaches the elongation force $F_{\mathrm{e}} \equiv \lim_{L\to\infty} f(L)$, which equals f_{p} in the case of a bare membrane as expected by ***Equation 4***. The existence of a force barrier in the f-L curve is similar to that in the tension-dominant condition ***Derényi et al.*** (***2002***). However, two striking differences should be noted: (i) in the pressure-dominant condition discussed here, a nonzero initiation force $F_{\mathrm{init}} \equiv f(L=0)$ is needed to merely maintain a flat membrane, i.e., to lift the membrane just off the cell wall (***Figure 2***e and f, diamonds), whereas in the tension-dominant condition, $F_{\mathrm{init}} = 0$ is independent of R_{b} (***Derényi et al., 2002***); (ii) when pressure dominates, the force barrier $F_{\max}$ significantly varies with the base radius R_{b} (***Figure 2***e and f, circles), whereas in the tension-dominant condition, $F_{\max}$ always overshoots 13% relative to the equilibrium force f_{σ} (***Derényi et al., 2002***), independent of R_{b}.

When comparing the differences between the f-L curves for the two BCs, we notice that: (i) the initiation force F_{init} scales with the base radius R_{b} as $F_{\mathrm{init}} = \frac{3}{8}\pi R_{\mathrm{b}}^2 p$ for the free-hinge BC, whereas $F_{\mathrm{init}} = \frac{1}{4}\pi R_{\mathrm{b}}^2 p$ for the fixed-hinge BC (***Figure 2***e and f, solid curves, see Derivation of the analytical solution for the initiation force); (ii) though the initiation force F_{init} is smaller for the fixed-hinge BC than for the free-hinge BC, the opposite trend is observed for the force barrier $F_{\max}$. The difference in $F_{\max}$ is more pronounced for smaller base radii. For instance, when $R_{\mathrm{b}} = 0.5 R_{\mathrm{p}}$, the force barrier $F_{\max}$ is about $4 f_{\mathrm{p}}$ for the free-hinge BC, while it is $7 f_{\mathrm{p}}$ for the fixed-hinge BC (***Figure 2***a and b, labeled by circles); (iii) The membrane neck appears at a smaller membrane height for the fixed-hinge BC than for the free-hinge BC. For instance, when $R_{\mathrm{b}} = 2R_{\mathrm{p}}$, the neck appears at a height of $3R_{\mathrm{p}}$ for the fixed-hinge BC, but $4R_{\mathrm{p}}$ for the free-hinge BC (***Figure 2***c and d, labeled by squares).

When the membrane is pulled up above the height of $6R_{\mathrm{p}}$, the force to elongate the tube remains almost unchanged $F_{\mathrm{e}} = f_{\mathrm{p}}$, regardless of the BCs and the base radii. However, the shape of the membrane can be quite different for different radii R_{b}. If $R_{\mathrm{b}} < R_{\mathrm{p}}$, the membrane exhibits a balloon-shape with a narrower base than the tubular body (***Figure 2***a and b, inset, labeled by triangles), whereas when $R_{\mathrm{b}} > R_{\mathrm{p}}$, a wider base connected to a narrower body is observed (***Figure 2***c and d, inset, labeled by triangles), which is more consistent with experimental observations (***Kukulski et al., 2012***).

For both BCs, the force barrier $F_{\max}$ is significantly reduced with increasing base radius R_{b}. When the base radius is increased from $0.5R_{\mathrm{p}}$ to $3R_{\mathrm{p}}$, the force barrier is reduced from $4f_{\mathrm{p}}$ to $1.5f_{\mathrm{p}}$ for the free-hinge BC, and from $7f_{\mathrm{p}}$ to $2f_{\mathrm{p}}$ for the fixed-hinge BC (***Figure 2***e, f, circles). These results suggest that a relatively wide base facilitates CME in yeast cells. With parameters listed in ***Table 2***, the force barrier to pull a membrane tube against a turgor pressure of 1 MPa can be reduced to 3000 pN for the free-hinge BC and 6000 pN for the fixed-hinge BC when the base radius R_{b} is greater than 30 nm (***Figure 2***e, f, circles). For the rest of the paper, we fix the base radius at $R_{\mathrm{b}} = 2R_{\mathrm{p}}$ and study the other factors that influence the membrane shape and the force to pull membrane up.

The ability of a fully-covered protein coat to reduce the force barrier and the initiation force depends on boundary conditions

In this section, we consider the effect of a uniform coat of curvature-generating proteins on membrane deformations. The ability of curvature-generating proteins to induce membrane curvature is characterized by the spontaneous curvature c_0 in the model. When the spontaneous curvature c_0 is small, e.g., $c_0 R_p = 0.2$, the f-L curves show similar trends as a barely coated membrane. However, a new branch of solutions with negative forces emerges (***Figure 3***a and b). On this branch, the membrane shape exhibits a highly curved Ω-shape, and terminates at a limiting shape of a closed spherical vesicle budding off from the base (***Figure 3***a and b, inset, labeled by pentagons). The free energy of the membrane on this negative-force branch is significantly higher than that on the positive-force branch (***Figure 3–Figure Supplement 1***a and b), thus being energetically unfavorable. Hereafter, the free energy refers to ***Equation 1*** excluding the contribution $-fL$ from the external pulling force.

When the spontaneous curvature c_0 is large, e.g., $c_0 R_p = 1$, the f-L curve breaks into two branches, each branch only covering part of the membrane height (***Figure 3***c and d). In the small-L branch, one L has two corresponding forces f. The larger f corresponds to a solution with a dome shape (***Figure 3***c and d, inset, labeled by circles), while the smaller f corresponds to a solution with an Ω-shape (***Figure 3***c and d, inset, labeled by hexagons). The dome-shape has lower free energy than the Ω-shape for the same membrane height L, and therefore is energetically more stable (***Figure 3–Figure Supplement 1***c and d). The large-L branch starts from a point at which the force f is slightly above zero, and the shape of the membrane is shown as a vesicle budding off from the base (***Figure 3***c and d, inset, labeled by pentagons). This implies that if a long tube is pulled out and maintained by a force, when the force is gradually released, the tube retracts and a vesicle spontaneously forms and detaches from the base of the membrane.

For a fully-coated membrane, increasing the spontaneous curvature c_0 is able to reduce the elongation force F_e. With increasing $c_0 R_p$ from 0 to 1, F_e shows exactly the same dependence on c_0 for both BCs and drops from f_p to about $0.2 f_p$ (***Figure 3***e and f, squares). However, The impact of the spontaneous curvature c_0 on the initiation force F_e and the force barrier F_{max} shows qualitative differences between the two BCs: (i) under the free-hinge BC, the initiation force F_{init} drops down with increasing c_0 and becomes negative for $c_0 R_p > 0.4$ (***Figure 3***e, diamonds and solid line). This negative F_{init} implies that the membrane is spontaneously bent off the cell wall without external forces. By contrast, under the fixed-hinge BC, the initiation force F_{init} remains positive and almost constant (***Figure 3***f, diamonds and solid line); (ii) the force barrier F_{max} noticeably decreases from $1.5 f_p$ to f_p with increasing c_0 under the free-hinge BC, while F_{max} remains almost constant at $2 f_p$ under the fixed-hinge BC (***Figure 3***e and f, circles).

In biological terms, our results suggest that for a membrane fully coated with curvature-generating proteins, increasing the spontaneous curvature c_0 might significantly reduce the force to lift the membrane up if the angle at the base is free to rotate, but a large amount of force is still needed to overcome the force barrier to pull a membrane tube. With the parameters listed in ***Table 2***, for the free-hinge BC, this force barrier can be reduced from 3000 pN for a barely coated membrane to 2000 pN for a fully-coated membrane (***Figure 3***e, circles). However, for the fixed-hinge BC, the protein coat has little impact on the force barrier, which is kept at 6000pN (***Figure 3***f, circles).

Partially coating the membrane with curvature-generating proteins can reduce the initiation force and the force barrier but not the elongation force

In this section, we study the inhomogenenous model where the membrane is coated with curvature-generating proteins only around the tip, thus mimicking the distribution of clathrin and other adaptor proteins. The spontaneous curvature in our model spatially varies as

$$c_0(a) = \frac{c_0}{2}\left\{1 - \tanh[\alpha(a - a_0)]\right\}, \tag{6}$$

where $a(s)$ is the surface area calculated from the tip to the position of arclength s. The parameter α controls the sharpness of the coating edge. The coating area of proteins is denoted by a_0, and these proteins induce a spontaneous curvature of c_0 in the coated region of the membrane. This form of spontaneous curvature has been used in many previous studies (***Agrawal and Steigmann, 2008***; ***Walani et al., 2015***; ***Hassinger et al., 2017***; ***Alimohamadi et al., 2018***).

We first vary the coating area a_0 while fixing the spontaneous curvature at $c_0 R_\mathrm{p} = 1$. When a_0 is small, the f-L curves are non-monotonic with a single force barrier F^1_max at a low membrane height, similar to that of a bare membrane. However, when a_0 is above a critical value, a second force barrier F^2_max emerges on the f-L curve at a higher membrane height where the membrane exhibits an Ω-shape (***Figure 4***a and b, inset, labeled by triangles). For $a_0/(2\pi R_\mathrm{p}^2) = 1$, the protein coat forms a hemispherical cap when the membrane is pulled up into a tubular shape (***Figure 4***a and b, inset, labeled by triangles). The initiation forces are negative for both BCs and the zero force $f = 0$ intersects with the f-L curve at a positive membrane height (***Figure 4***a and b, inset, labeled by circles). For very large coating area ($a_0/(2\pi R_\mathrm{p}^2) = 2$), the membrane is almost fully coated with proteins when the membrane is flat (***Figure 4***c, inset, labeled by circles). The f-L curve is broken into two branches, each branch only covering part of the membrane height (***Figure 4***c and d), similar to the f-L curve of a fully-coated membrane. For the free-hinge BC, the zero force $f = 0$ intersects with the f-L curve at three points, two of them lying on the small-L branch and the third one on the large-L branch (***Figure 4***c, inset, labeled by circles and squares in the small-L branch and triangles in the large-L branch). The two points on the small-L branch correspond to a dome-shape of low free energy and a tubular shape of high free energy (***Figure 4–Figure Supplement 1***c, circles and squares). Therefore, in the absence of forces, the membrane adopts a flat dome-shape, spontaneously bent off the cell wall. The one point on the large-L branch corresponds to a highly curved Ω-shape with a narrow neck (***Figure 4***c, inset, labeled by triangles), which is the final shape of a long membrane tube when it retracts upon force release. The large-L branch starts with a limiting membrane shape that is a closed vesicle budding off from the base (***Figure 4***c, inset, labeled by pentagons). In contrast with the fully-coated membrane, the force at this point is negative, which means that a downward force is further needed to push the membrane into a budding vesicle when the membrane tube retracts. Under the fixed-hinge BC, the f-L curve for ($a_0/(2\pi R_\mathrm{p}^2) = 2$) shows similar features with that of the free-hinge BC, except that the flat dome-shaped solution at $f = 0$ does not exist (***Figure 4***d). This is because the initiation force F_init is positive and the membrane cannot be spontaneously bent off the cell wall.

Despite some common features in the f-L curves for both BCs, differences also exist: (i) under the free-hinge BC, the initiation force F_init decreases and remains negative with increasing a_0, whereas under the fixed-hinge BC, F_init is negative for intermediate values of a_0, and becomes positive for larger a_0 (***Figure 4***e and f, diamonds); (ii) a similar difference is also observed for the low-height force barrier F^1_max, which is monotonically decreasing with a_0 under the free-hinge BC, whereas it is non-monotonic under the fixed-hinge BC (***Figure 4***e and f, circles).

For a partially coated membrane, the low-height force barrier F^1_max can be significantly reduced to below f_p for some coating areas (***Figure 4***e and f, circles), whereas the high-height force barrier F^2_max increases with a_0 and remains above f_p (***Figure 4***e and f, pentagons). This is because the force barrier F^2_max must be greater than the elongation force F_e, which equals f_p for both BCs and any coating areas. This trade off between the two force barriers implies there is an optimum coating area that minimizes the overall force barrier. With the parameters listed in ***Table 2***, the optimum coating area is about $1500\ \mathrm{nm}^2$ for both BCs. The minimum force barrier is about $2000\ \mathrm{pN}$ for the free-hinge BC, and about $3500\mathrm{pN}$ for the fixed-hinge BC. Compared with the force barrier of $6000\mathrm{pN}$ for a fully-coated membrane under the fixed-hinge BC, partially coating the membrane significantly reduces the force barrier.

Increasing the spontaneous curvature of partially coated membrane leads to a sharp transition of the membrane shape.

In this section, we vary the spontaneous curvature c_0 while fixing the coating area ($a_0/(2\pi R_p^2) = 1$) to study how c_0 influences the f-L curves for a partially coated membrane. Upon gradually increasing c_0, the f-L curve shows similar trends to what we observed when increasing the coating area. Above a critical value of c_0, a high-height force barrier $F_{\max}^2$ appears on the f-L curve in addition to the low-height force barrier $F_{\max}^1$ (***Figure 5***a and b). Further increasing the spontaneous curvature c_0 splits the f-L curve into two branches, a small-L branch and a large-L branch (***Figure 5***c and d). A striking new feature is that when $c_0 R_p = 2$, the force for the entire small-L branch falls below zero (***Figure 5***c and d). The zero force $f = 0$ intersects with the f-L curve on the long-L branch at only one point, which corresponds to a highly curved Ω-shape (***Figure 5***c and d, inset, labeled by squares). This shape has the lowest free energy (***Figure 5–Figure Supplement 1***c and d, labeled by squares), which implies that even in the absence of forces, increasing the spontaneous curvature c_0 can lead to a transition of the membrane from the dome-shape in the small-L branch to the Ω-shape in the large-L branch. The membrane height has a sharp increase during this transition.

Both the low-height force barrier $F_{\max}^1$ and the initiation force F_{init} linearly decrease with increasing c_0 (***Figure 5***e and f, circles and diamonds), and they become negative when c_0 is beyond a critical value. By contrast, the high-height force barrier $F_{\max}^2$ linearly increases with c_0 (***Figure 5***e and f, pentagons), and remains above f_p. The optimum spontaneous curvature, which has the minimum force barrier, is about $0.8R_p^{-1}$ for both BCs. The corresponding force barrier is as much as f_p, which is the lowest force barrier one can achieve by partially coating the membrane with curvature-generating proteins. With the parameters listed in ***Table 2***, the optimum spontaneous curvature corresponds to a preferred radius of about 20nm. The force barrier for the free-hinge BC is about 2000pN, and for the fixed-hinge BC is about 3500pN.

Our theory agrees well with experiments.

To validate our theory, we compare the shapes calculated with our model with experimental shapes of endocytic invaginations in budding yeast imaged with electron tomography (***Kukulski et al., 2012***). Based on the observation that the coating area of clathrin molecules remains constant during CME (***Avinoam et al., 2015***) and the number of clathrin molecules fits a hemispherical cap (***Sirotkin et al., 2010***), we assume a coating area of proteins $a_0 = 2\pi R_p^2$, and these proteins induce an isotropic curvature $c_0 = 1/R_p$. The characteristic radius R_p is used as a fitting parameter such that the membrane neck is absent until the membrane height reaches $L = 42\text{nm}$ as observed experimentally.

First, we group the experimental membrane shapes into three sets according to their heights and overlay them at the tip. Our calculated membrane shapes agree well with the experimental data, particularly in the early stage when the membrane height is low (***Figure 6***a and b). For membrane shapes that are higher than $65\ \text{nm}$, experimental membrane shapes are typically asymmetric and exhibit a narrower neck than the calculated ones, probably due to the presence of other membrane proteins that arrive later during CME and impose a cylindrical curvature at the neck of the invagination (e.g. amphiphysins). These effects are not considered in our model.

We also consider two geometric features of the membrane shapes, the tip radius R_t and the tip-neck distance D_t, and compare these features between results calculated by our model and measured from experiments. The tip radius R_t is defined as the reciprocal of the meridian curvature ψ averaged over an arc that extends over $15\ \text{nm}$ from the endocytic invagination tip (***Kukulski et al., 2012***). The tip-neck distance D_t is defined as the vertical distance between the neck and the tip. Experimental data shows that the tip radius R_t drops from $50-100\text{nm}$ to 15nm as the membrane height increases. Our theory matches the trend of the experimental data, particularly for the part where $R_t < 40\ \text{nm}$ (***Figure 6***c and d). As for the tip-neck distance D_t, our theory predicts that D_t grows slowly with the membrane height L when L is less than $65\ \text{nm}$. Beyond this point, D_t scales almost linearly with L with a larger slope than the initial phase. This theoretical prediction again

matches well with the experimental data (***Figure 6***e and f). Though both BCs can fit the experimental data, the fitting parameters R_p are different. For the free-hinge BC, one gets $R_p = 15\text{nm}$ and for the fixed-hinge BC $R_p = 18\text{nm}$. This leads to a large difference in the magnitude of forces in the f-L curve for the two BCs (***Figure 6***g and h). For the free-hinge, the force barrier is about $2000\ \text{pN}$, while for the fixed-hinge, it is about $3500\ \text{pN}$.

Discussion

Fixed base v.s. freely moving base.

In this paper, we have studied membrane deformations driven by a point force and by curvature-generating proteins in the presence of a high turgor pressure. We have focused on BCs where the base radius of the membrane is fixed. For a membrane fully coated with curvature-generating proteins, the initiation force F_{init} either decreases with the intrinsic curvature c_0 under the free-hinge BC, or is independent of c_0 under the fixed-hinge BC (***Figure 3***e and f, diamonds and solid lines). A previous work studied a similar homogeneous model but used a BC of a freely moving base and fixed-hinge BC (BC4 in ***Table 1***, ***Dmitrieff and Nédélec*** (***2015***)). This BC led to the surprising conclusion that the initiation force F_{init} of a fully coated membrane is proportional to the spontaneous curvature c_0, which implies that increasing the spontaneous curvature c_0 hinders CME because it raises the force required to lift the membrane off the cell wall. In addition, as a result of the freely moving base, the model predicted that the base radius R_b approaches zero when the membrane height is low. This result is inconsistent with experimental observations that the base radius of membrane invaginations remains roughly the same during the entire course of CME, from shallow invaginations to long tubes (***Figure 6***a and b). Therefore the experimental data supports our assumption that the base of the membrane is maintained at a fixed radius by endocytic proteins or by attachment to the cell wall. A recent systematic study of proteins involved in endocytosis by super-resolution microscopy revealed that many proteins are organized in concentric rings around the clathrin coat (***Mund et al., 2018***). These proteins may serve as anchors and may fix the base radius of the endocytic membrane.

The different dependence of the initiation force F_{init} on c_0 between fixed-base BC and freely-moving-base BC can be clarified with a simple example. Since F_{init} is only related to the early stage of CME when the membrane is almost flat, we approximate the dome-shaped membrane as a spherical cap and calculate its free energy $E(R; c_0, R_b)$ as a function of the sphere radius R for different spontaneous curvatures c_0 and base radii R_b (***Figure 7***). For the fixed-base BC, the base radius R_b is a constant. When c_0 is small, $E(R; c_0, R_b)$ decreases monotonically with R and has its minimum at $R = \infty$, which implies that a flat shape is more favorable than a curved one (***Figure 7***a). When c_0 becomes large, $E(R; c_0, R_b)$ has a nontrivial minimum at a finite radius R (***Figure 7***b,$R_b = 2R_p$), which implies that the membrane spontaneously bends into a curved shape. However, for the freely-moving-base BC assumed in the work of ***Dmitrieff and Nédélec*** (***2015***), the base radius R_b becomes a free parameter and the free energy $E(R, R_b; c_0)$ is a function of both R and R_b. No matter how large c_0 is, the energy $E(R, R_b; c_0)$ always admits a trivial minimum at $R_b = 0$, which represents a solution without any deformation (***Figure 7***a and b,$R_b = 0R_p$). If a force f is applied, a nontrival minimum of the total free energy $F(R, R_b; f, c_0) = E(R, R_b; c_0) - f\,L(R, R_b)$ may exist for a positive force f (***Figure 7–Figure Supplement 1***). However, the base radius for this nontrivial minimum is unrealistically narrow ($\sim 0.02\text{nm}$,see Spherical cap approximation), therefore a freely moving base is probably not a proper BC to model CME in yeast.

Free-hinge v.s. fixed-hinge.

Our analysis of the experimental data favors the BC with fixed base radius over that with freely moving base. However, we cannot directly distinguish whether the angle of the membrane at the base is free to rotate (free-hinge) or fixed to zero (fixed-hinge), since both BCs show good agreements with the experimental data (***Figure 6***a-f). Under the free-hinge BC, the membrane

shape has a kink at the base points. We stress that this discontinuity in the membrane angle is physically and biologically plausible. First, for a membrane fully-coated with curvature generating proteins, the membrane's spontaneous curvature can change abruptly at the base points and such discontinuity of the mechanical properties of the membrane will result in a kink. Second, for a partially-coated membrane whose mechanical properties smoothly change across the base points, the kink can be induced by external factors. Though it is hypothetical, early arriving endocytic proteins, such as myosin-I motors and BAR-domain proteins Syp1p, Cdc15p and Bzz1p which form a ring-like structure around the clathrin-coated pit, can serve such a purpose (***Mund et al., 2018***). They may fix the base radius, impose the angle of the membrane outside of the invagination, and let the membrane inside the invagination freely rotate, therefore forming a kink.

Actin polymerization alone is insufficient to overcome the force barrier for CME in yeast cells even with the help of proteins that induce membrane curvature

One of the key questions we aimed to address in this paper is how much force is needed to pull a membrane tube against high turgor pressure during CME in yeast cells. Though we can fit the experimental data with both the free-hinge BC and the fixed-hinge BC, there is a difference in the fitting parameter R_{p}, which is $15\ \mathrm{nm}$ for the free-hinge BC and $18\ \mathrm{nm}$ for the fixed-hinge BC. This small difference in R_{p} results in a big difference in the force barrier for CME as the force scales with R_{p}^2. For the free-hinge BC, the force barrier is about $2000\ \mathrm{pN}$, but for the fixed-hinge, it is about $3500\ \mathrm{pN}$ (***Figure 6***g and h). However, even $2000\mathrm{pN}$ is still beyond the force ($< 200\mathrm{pN}$) that can be generated by polymerization alone of $150-200$ actin filaments at the endocytic site (***Sirotkin et al., 2010***; ***Berro et al., 2010***), given that the measured polymerization force for a single filament is only $1\mathrm{pN}$ and the force generated by a bundle of filaments is usually smaller than the sum of each individual ones (***Footer et al., 2007***). Investigating non-polymerization based force production by the actin machinery will be our future work. A possible way is to release the elastic energy stored in geometrically frustrated crosslinkers, such as fimbrin ***Ma and Berro*** (***2018***, 2019).

Methods and materials

Derivation of the membrane shape equations.

The membrane shape is parameterized with its meridional coordinates $[R(s), Z(s)]$, which are related to the tangent angle $\psi(s)$ via the goemetrical relation:

$$\dot{R} = \cos\psi, \qquad \dot{Z} = -\sin\psi. \tag{7}$$

In order to obtain the Euler-Lagrange equation associated with the free energy ***Equation 1***, we express $\mathcal{F}$ in ***Equation 2*** explicitly as

$$\mathcal{F} = \frac{\kappa}{2}R(\dot{\psi} + \frac{\sin\psi}{R} - c_0)^2 + \sigma R + \frac{pR^2}{2}\sin\psi - \frac{f}{2\pi}\sin\psi + \gamma(\dot{R} - \cos\psi). \tag{8}$$

Here we introduce the Lagrangian multiplier $\gamma(s)$ to impose the geometric constraint set by ***Equation 7***. The variation of the functional F in ***Equation 2*** reads

$$\begin{aligned}\frac{\delta F}{2\pi} &= \int_0^S \mathrm{d}s\left\{\left[\frac{\partial\mathcal{F}}{\partial\psi} - \frac{\mathrm{d}}{\mathrm{d}s}\frac{\partial\mathcal{F}}{\partial\dot{\psi}}\right]\delta\psi + \left[\frac{\partial\mathcal{F}}{\partial R} - \frac{\mathrm{d}}{\mathrm{d}s}\frac{\partial\mathcal{F}}{\partial\dot{R}}\right]\delta R + \frac{\partial\mathcal{F}}{\partial\gamma}\delta\gamma\right\} \\ &+ \frac{\partial\mathcal{F}}{\partial\dot{\psi}}\delta\psi\Big|_{s=0}^{s=S} + \frac{\partial\mathcal{F}}{\partial\dot{R}}\delta R\Big|_{s=0}^{s=S},\end{aligned} \tag{9}$$

which contains both the bulk terms (first line) and the boundary terms (second line). The Euler-Lagrange equations can be obtained by the vanishing bulk terms, which are reduced to

$$\ddot{\psi} = \frac{\cos\psi\sin\psi}{R} - \frac{\dot{\psi}}{R}\cos\psi + \frac{p}{2\kappa}R\cos\psi + \frac{\gamma}{R}\sin\psi - \frac{f}{2\pi\kappa R}\cos\psi, \tag{10}$$

and

$$\dot{\gamma} = \frac{1}{2}\kappa(\dot{\psi} - c_0)^2 - \frac{\kappa\sin^2\psi}{2R^2} + \sigma + pR\sin\psi, \tag{11}$$

as well as ***Equation 7***.

For the homogeneous model, the spontaneous curvature c_0 is uniform and $\mathcal{F}$ is explicitly independent of the arclength s. This symmetry leads to a conserved quantity (***Jülicher and Seifert, 1994***)

$$H \equiv \frac{\kappa}{2} R \left[\dot{\psi} - \left(\frac{\sin\psi}{R} - c_0 \right)^2 \right] - \frac{p}{2} R^2 \sin\psi - \sigma R + \gamma \cos\psi + \frac{f}{2\pi} \sin\psi = 0. \tag{12}$$

For the inhomogeneous model, the spontaneous curvature $c_0(s)$ is spatially varied over the arclength as depicted by ***Equation 6***. To ensure that H is still conserved, i.e., $\dot{H} = 0$, the membrane tension σ is no longer a constant but spatially varies as

$$\dot{\sigma} = \kappa \left(\frac{\sin\psi}{R} + \dot{\psi} - c_0 \right) \dot{c_0}. \tag{13}$$

Equation 13 is essentially equivalent to the constraint that the membrane area is locally unstretchable (***Agrawal and Steigmann, 2008***).

Derivation of the boundary conditions.

In order to get proper BCs, we set the boundary terms in ***Equation 9*** to zero. At the membrane tip ($s = 0$), $R = 0$ by definition and we choose $\psi = 0$ to avoid any singularity. As a result, $\delta R = 0$ and $\delta\psi = 0$ and the boundary terms automatically vanish.

At the base of the invagination ($s = S$), as a result of the product of two conjugate variables $\frac{\partial \mathcal{F}}{\partial \dot{\psi}}$ and $\delta\psi$, we have the freedom to let either $\frac{\partial \mathcal{F}}{\partial \dot{\psi}} = 0$, i.e. the membrane can be freely rotate (free-hinge BC), or $\delta\psi = 0$, i.e. the angle of the membrane is fixed (fixed-hinge BC). Similarly, we can choose $\frac{\partial \mathcal{F}}{\partial \dot{R}} = 0$, i.e. the base can freely move, or $\delta R = 0$, i.e. the base radius is fixed. The combination of the two choices make up the four possible BCs listed in ***Table 1***.

Numerical methods to calculate the force-height (f-L) relationships

Eqs. (10), (11) and (13) have a singular point at $R = 0$. In order to avoid the singular point, we set $R(s = 0) = \epsilon R_{\mathrm{p}}$, where $\epsilon = 0.001$ is a small number. For the homogeneous model with a uniform spontaneous curvature c_0, Eqs. (7), (10) and (11) are numerically integrated from $s = 0$ with MATLAB solver ode45 until the free-hinge BC or the fixed-hinge BC is met. The initial value of $\gamma(s = 0)$ is obtained from the conserved quantity H in ***Equation 12***. For a particular height L_0, the initial curvature $\dot{\psi}(s = 0)$ and the force f are tuned to match $R = R_{\mathrm{b}}$ and $L = L_0$ at the base, and we can then calculate the f-L curve and the corresponding membrane shapes. For the inhomogeneous model with a spatially varied spontaneous curvature $c_0(s)$ defined by ***Equation 6***, Eqs. (7),(10), (11), (13), and $\dot{a} = 2\pi R$ are numerically integrated until the boundary condition is met. The combination of $\dot{\psi}(s = 0), \sigma(s = 0), f$ are tuned to match $R = R_{\mathrm{b}}$, $L = L_0$ and $\sigma = \sigma_0$ at the base.

Acknowledgments

This research is supported by National Institutes of Health/National Institute of General Medical Sciences Grant R01GM115636. We thank Wanda Kukulski, Marko Kaksonen and John Briggs for kindly sharing the micrograph of ***Figure 1***a. We thank Dr. Pablo Sartori for critical reading of the manuscript.

Competing interests

The authors do not have any competing interest.

References

Aghamohammadzadeh S, Ayscough KR. Differential requirements for actin during yeast and mammalian endocytosis. Nature Cell Biology. 2009; 11(8):1039–1042. https://doi.org/10.1038/ncb1918, doi: 10.1038/ncb1918.

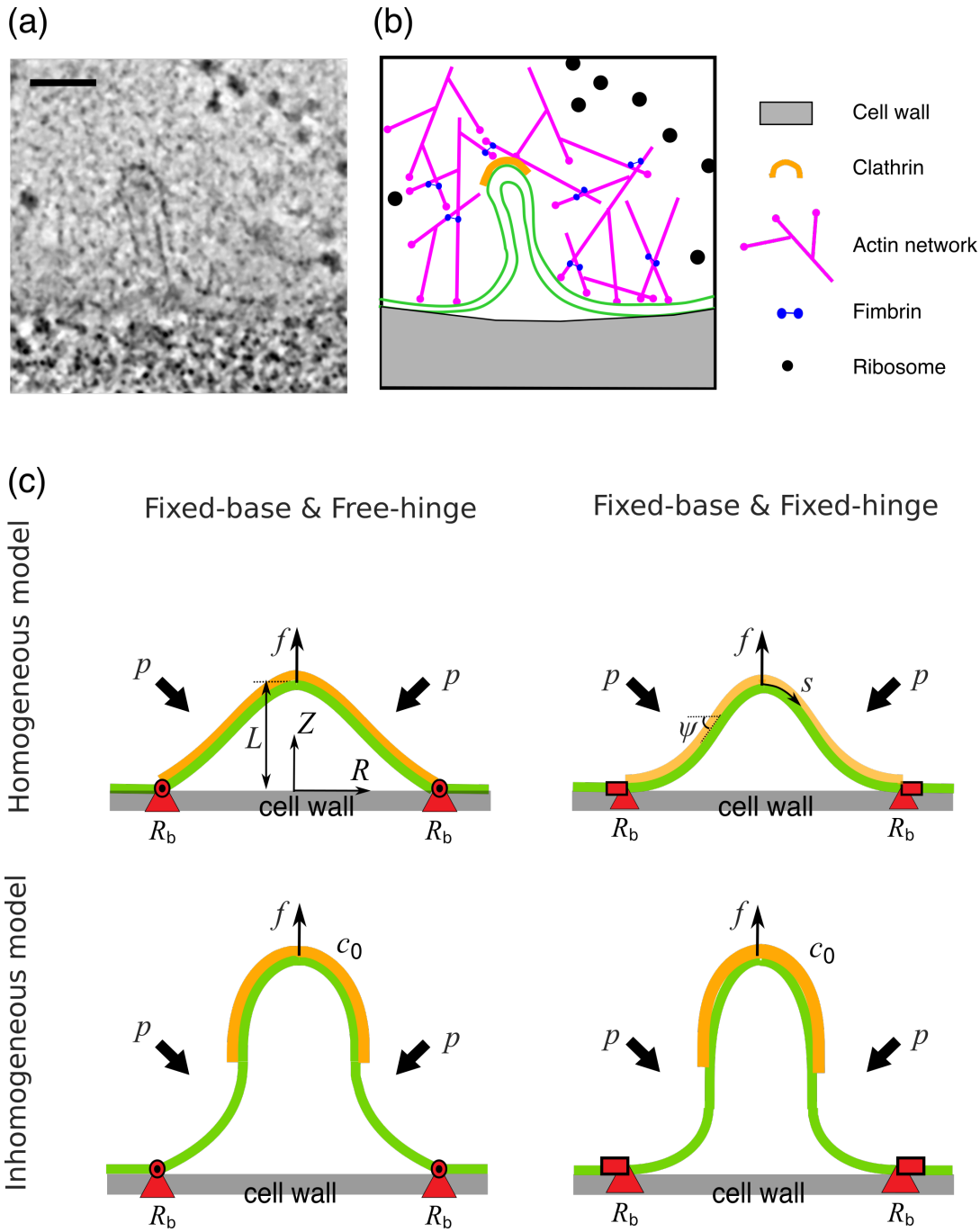

Figure 1. CME in yeast and membrane models for CME. (a) Electron micrograph of a membrane tube formed during CME in budding yeast. The image was obtained from https://www.embl.de/download/briggs/endocytosis.html and adapted under the permission of the authors in ***Kukulski et al.*** (***2012***). The scale bar is 50nm. (b) Schematic illustration of the membrane and key endocytoic proteins shown in (a). The actin network surrounding the membrane tube is depicted as meshwork of branched and crosslinked filaments, though their precise organisation cannot be resolved in the electron micrograph and the meshwork appears as a zone from which ribosomes are excluded. A clathrin coat covering the tip of the membrane tube is also depicted, though the specific spatial distribution of clathrin molecules cannot be resolved in (a). (c) Illustration of the membrane models. The membrane (green layer) is pulled up by a point force f against osmotic pressure p. The membrane is coated with proteins (orange layer) that locally change the spontaneous curvature of the membrane c_0. The position of the base (red triangles) is maintained at a constant value R_b. We consider a homogeneous model (top) where the membrane is fully-coated or barely-coated with curvature-generating proteins, and an inhomogeneous model (bottom) where the membrane is partially-coated. We consider two types of BCs, the free-hinge BC (left) where the membrane is allowed to freely rotate at the base, and the fixed-hinge BC (right) where the membrane angle is fixed.

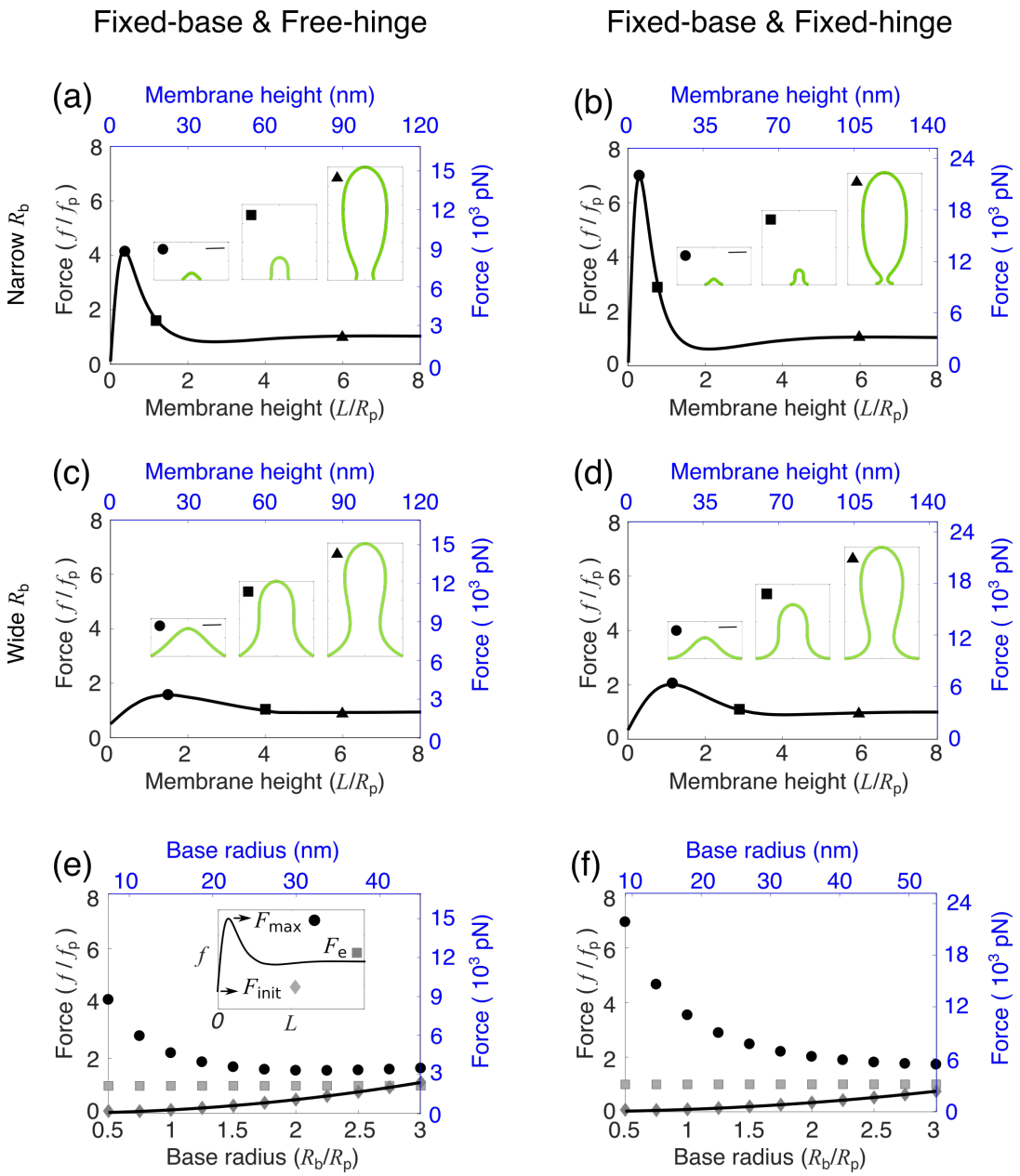

Figure 2. Effect of the base radius R_b on the membrane shape and force requirement. (a - d) Force-height relationship f-L of membrane deformations for a fixed base radius $R_b/R_p = 0.5$ in (a, b) and $R_b/R_p = 2$ in (c, d), where R_p is the characteristic tube radius (***Equation 4***). The spontaneous curvature $c_0 R_p = 0$. Insets show membrane shapes at the points indicated by the corresponding symbols on the f-L curve. The square indicates the critical shape where the membrane is about to form a neck. The scale bar corresponds to the characteristic tube radius R_p. (e, f) Force barrier F_{max} (circle), initiation force F_{init} (diamond) and elongation force F_e (square) for varying base radii R_b. The solid curve represents the analytical solution for F_{init}. (a-f) In the left column (a, c, e), the free-hinge BC is imposed at the base points $R = R_b$, while in the right column (b, d, f), the fixed-hinge BC is imposed. On the left and bottom axes (black), non-dimensionalized quantities are used, while on the right and top axes (blue), quantities are measured in their physical units. The parameters are listed in ***Table 2***.

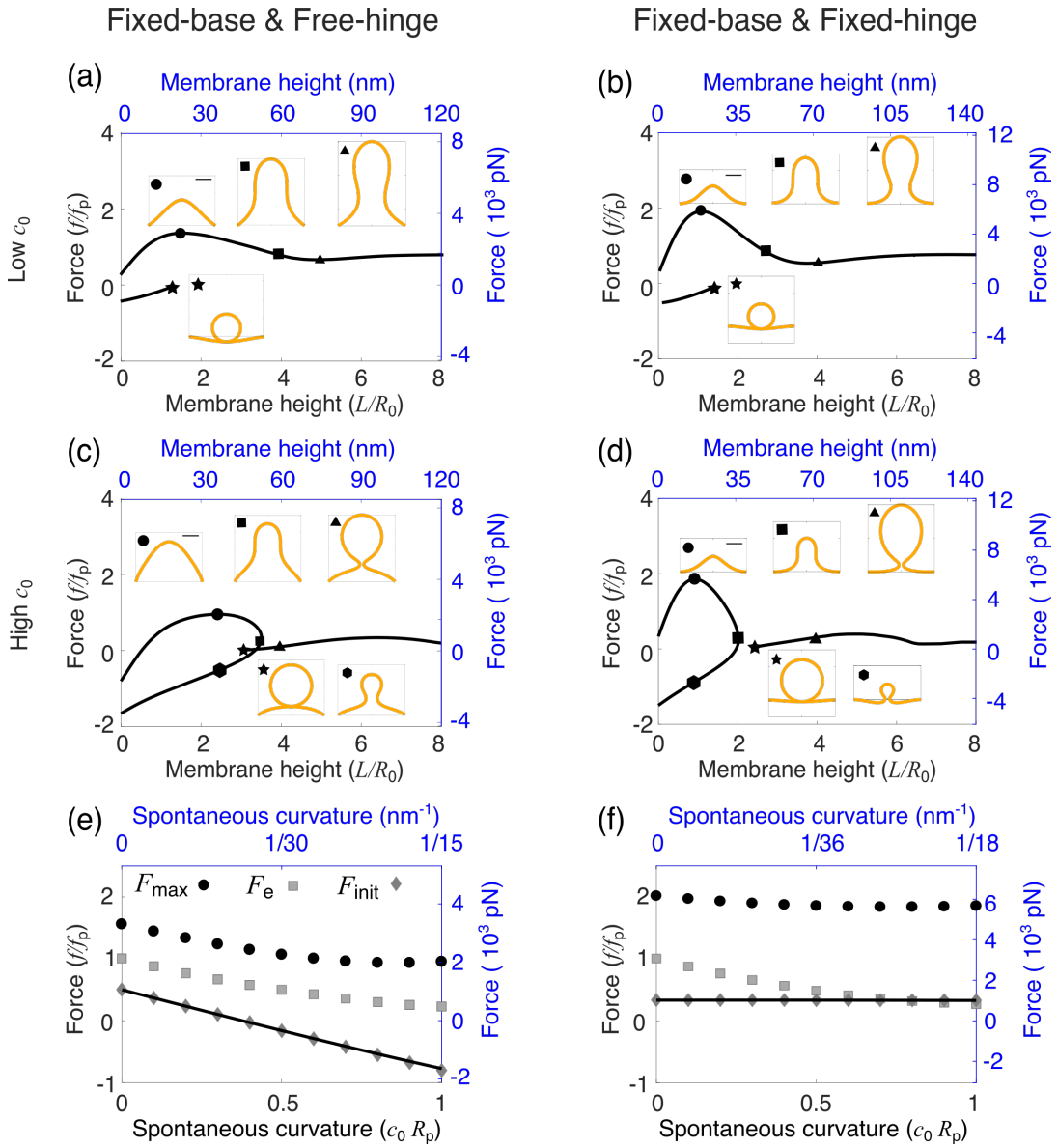

Figure 3. Effect of the spontaneous curvature c_0 on membrane shape and force requirement for a fully coated membrane. (a - d) Force-height (f-L) relationship of membrane deformations for a fixed spontaneous curvature $c_0 R_p = 0.2$ in (a, b) and $c_0 R_p = 1$ in (c, d). Insets show membrane shapes at the points indicated by the corresponding symbols on the f-L curve. The square indicates the critical shape where the membrane is about to form a neck. The scale bar corresponds to R_p. (e, f) Force barrier F_{max} (circle), initiation force F_{init} (diamond) and elongation force F_e (square) for varying c_0. The solid curve represents the analytical solution for F_{init}. (a - f) In the left column (a, c, e), the free-hinge BC is imposed at the base points $R_b = 2R_p$, while in the right column (b, d, f), the fixed-hinge BC is imposed. On the left and bottom axes (black), non-dimensionalized quantities are used, while on the right and top axes (blue), quantities are measured in their physical units. The parameters are listed in ***Table 2***.

Figure 3–Figure supplement 1. Free energy of membrane deformations.

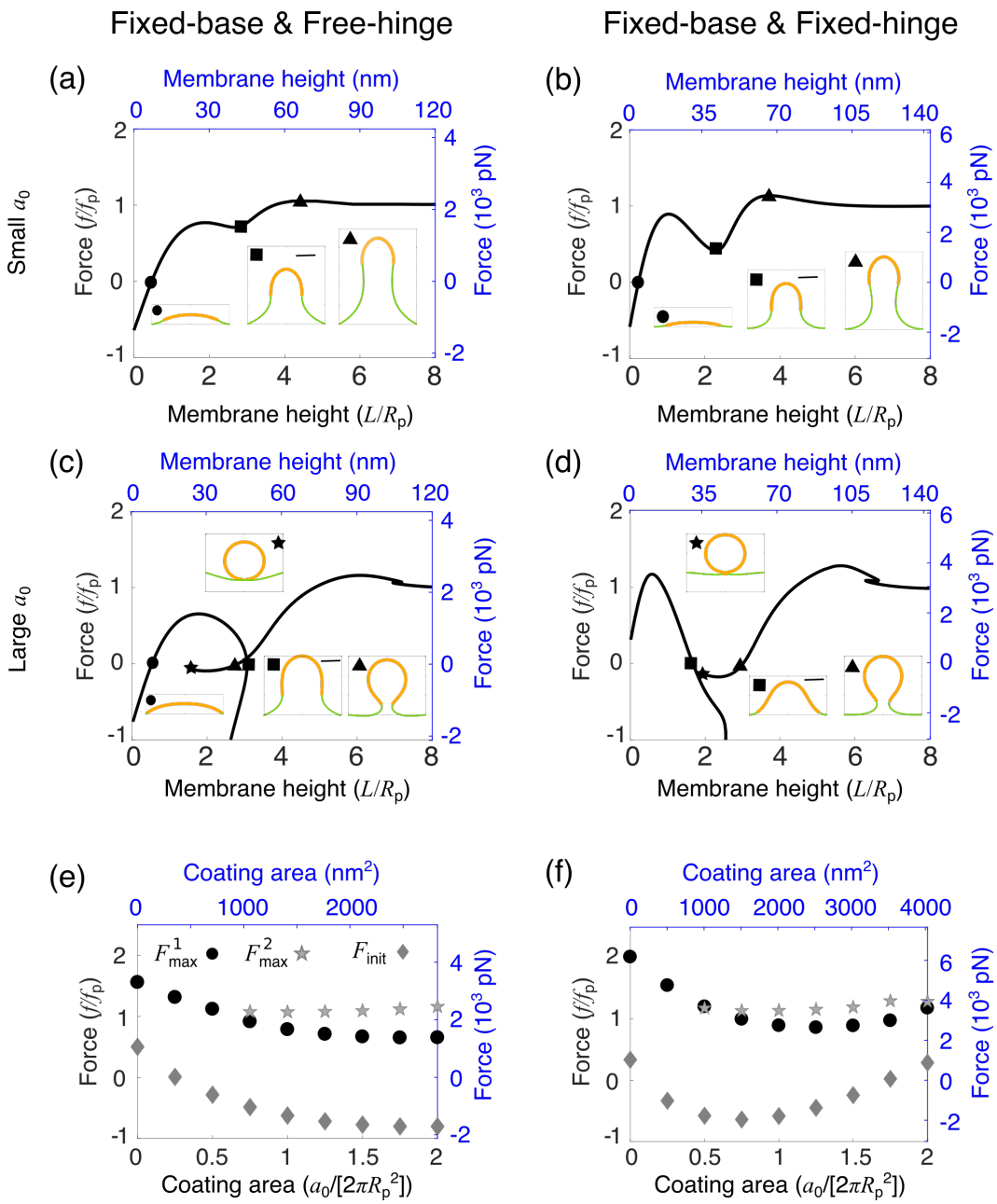

Figure 4. Effect of the coating area a_0 of curvature-generating proteins on membrane shape and force requirement for a partially coated membrane. (a - d) Force-height (f-L) relationship of membrane deformations for a fixed coating area $a_0/(2\pi R_p^2) = 1$ in (a, b) and $a_0/(2\pi R_p^2) = 2$ in (c, d). Insets show membrane shapes at the points indicated by the corresponding symbols on the f-L curve. The orange part represents the area of the membrane coated with proteins and the green part represents the bare membrane. The scale bar corresponds to R_p. (e, f) Low-height force barrier F^1_{max} (circle), high-height force barrier F^2_{max} (pentagon) and initiation force F_{init} (diamond) for varying a_0. (a - f) In the left column (a, c, e), the free-hinge BC is imposed at the base points $R_b = 2R_p$, while in the right column (b, d, f), the fixed-hinge BC is imposed. On the left and bottom axes (black), non-dimensionalized quantities are used, while on the right and top axes (blue), quantities are measured in their physical units. The parameters are listed in ***Table 2***.

Figure 4–Figure supplement 1. Free energy of membrane deformations.

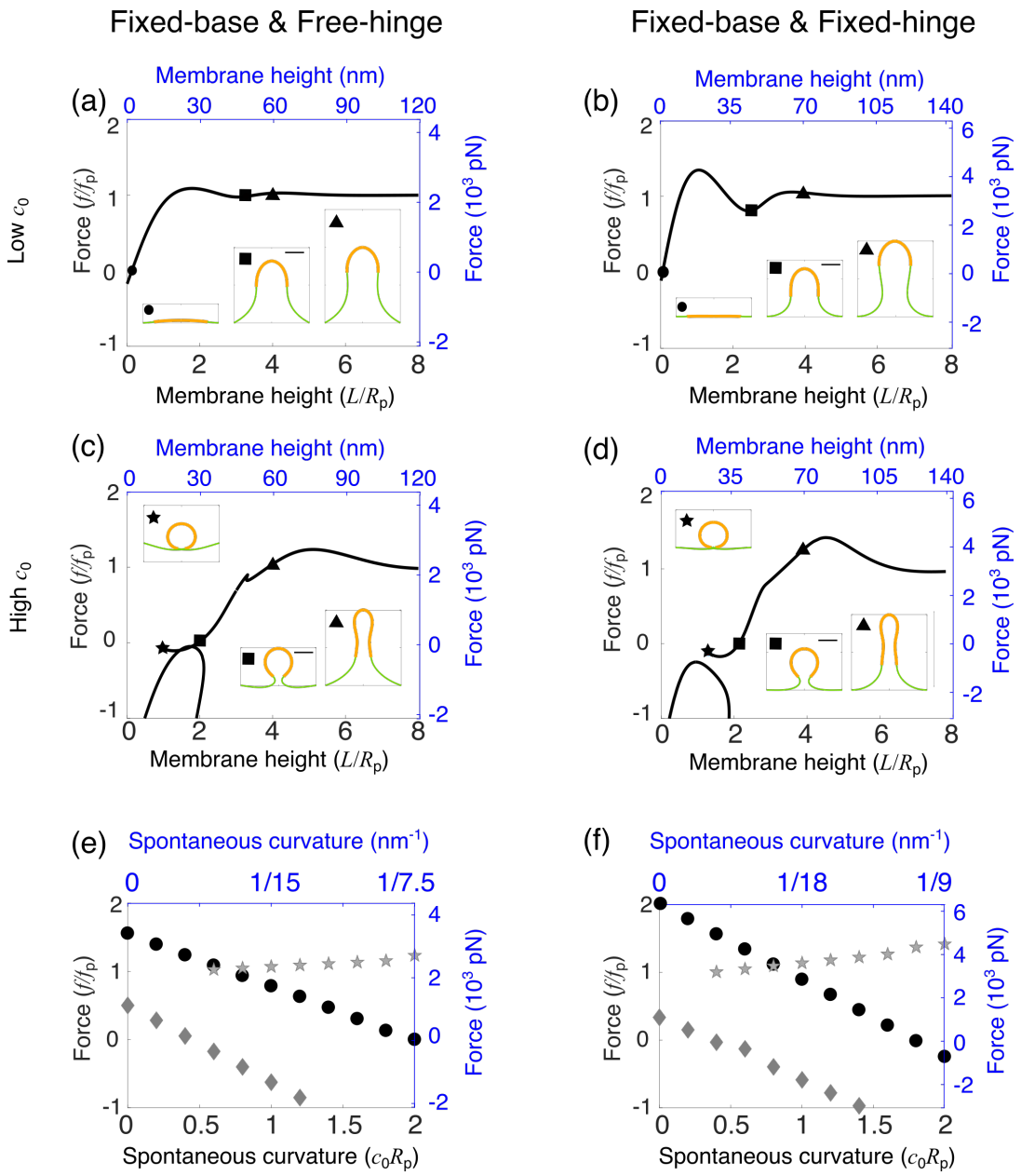

Figure 5. Effect of the spontaneous curvature c_0 of curvature-generating proteins on membrane shape and force requirement for a partially coated membrane. (a - d) Force-height (f-L) relationship of membrane deformations for a fixed spontaneous curvature $c_0R_p = 0.6$ in (a, b) and $c_0R_p = 2$ in (c, d). Insets show membrane shapes at the points indicated by the corresponding symbols on the f-L curve. The orange part represents the area of the membrane coated with proteins and the green part represents the bare membrane. The scale bar corresponds to R_p. (e, f) Low-height force barrier F^1_{max} (circle), high-height force barrier F^2_{max} (pentagon) and initiation force F_{init} (diamond) for varying c_0. (a - f) In the left column (a, c, e), the free-hinge BC is imposed at the base points $R_b = 2R_p$, while in the right column (b, d, f), the fixed-hinge BC is imposed. On the left and bottom axes (black), non-dimensionalized quantities are used, while on the right and top axes (blue), quantities are measured in their physical units. The parameters are listed in ***Table 2***.

Figure 5–Figure supplement 1. Free energy of membrane deformations.

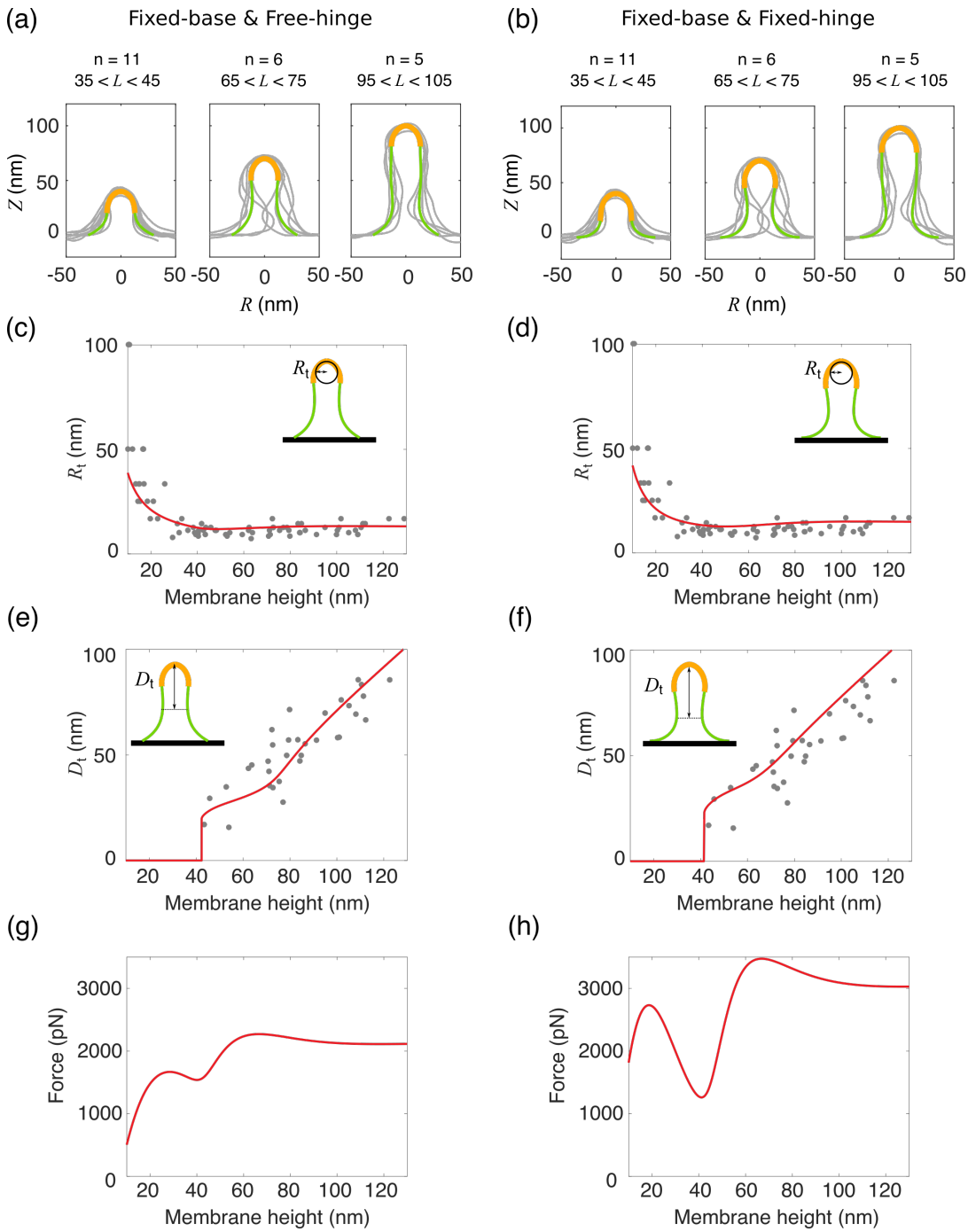

Figure 6. Comparison between our theory and experiments. (a, b) Membrane shapes obtained by electron tomography are grouped according to their heights and overlaid at the tip. The data come from ***Kukulski et al.*** (***2012***). The membrane shapes obtained by our model are represented by solid curves. The orange part represents the area of the membrane coated with proteins and the green part represents the bare membrane. (c, d) Comparison of the tip radius R_t between obtained with our theory (line) and measured experimentally (dots). (e, f) Comparison of the neck to tip distance D_t between obtained with our theory (line) and measured experimentally (dots). (g, h) Prediction of the force-height (f-L) relationship from our theory using the parameters listed in ***Table 2*** which fit the experimental shapes in (a, b). (a-h) In the left column (a, c, e, g), the free-hinge BC is imposed at the base points $R_b = 30$ nm, while in the right column (b, d, f, h), the fixed-hinge BC is imposed at the base points $R_b = 36$ nm.

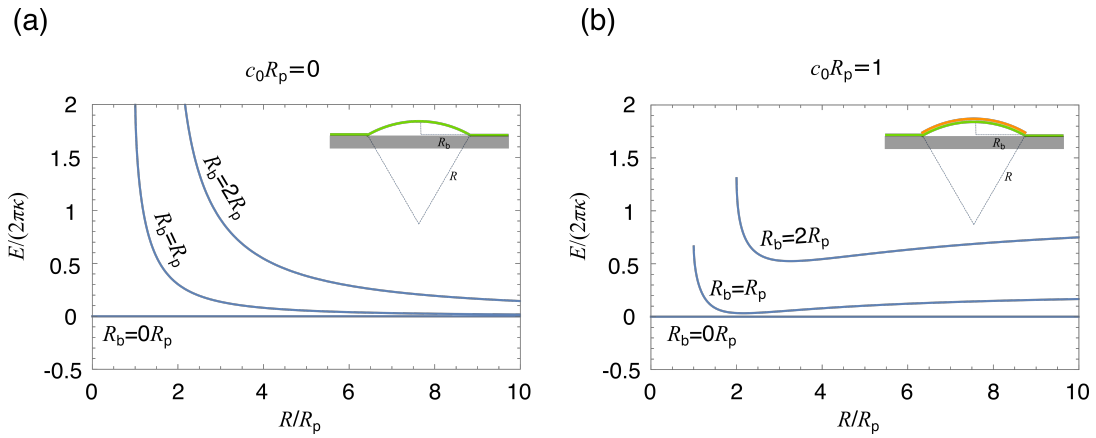

Figure 7. Free energy of membrane deformations under spherical cap approximation (a, b) Free energy of the membrane as a function of the sphere radius R for $c_0R_p = 0$ in (a) and $c_0R_p = 1$ in (b). For different base radii R_b, the range of R is $[R_b, \infty]$, where $R = R_b$ corresponds to a hemi-spherical cap and $R = \infty$ corresponds to a flat shape.

Figure 7–Figure supplement 1. Free energy of membrane deformations in the presence of external force under spherical cap approximation.

Agrawal A, Steigmann DJ. Modeling protein-mediated morphology in biomembranes. Biomechanics and Modeling in Mechanobiology. 2008 Nov; 8(5):371. https://doi.org/10.1007/s10237-008-0143-0, doi: 10.1007/s10237-008-0143-0.

Alimohamadi H, Vasan R, Hassinger JE, Stachowiak JC, Rangamani P. The role of traction in membrane curvature generation. Molecular biology of the cell. 2018; 29(16):2024–2035.

Atilgan E, Magidson V, Khodjakov A, Chang F. Morphogenesis of the Fission Yeast Cell through Cell Wall Expansion. Current Biology. 2015 2018/12/25; 25(16):2150–2157. https://doi.org/10.1016/j.cub.2015.06.059, doi: 10.1016/j.cub.2015.06.059.

Avinoam O, Schorb M, Beese CJ, Briggs JAG, Kaksonen M. Endocytic sites mature by continuous bending and remodeling of the clathrin coat. Science. 2015; 348(6241):1369–1372. http://science.sciencemag.org/content/348/6241/1369, doi: 10.1126/science.aaa9555.

Basu R, Munteanu EL, Chang F. Role of turgor pressure in endocytosis in fission yeast. Molecular biology of the cell. 2014 03; 25(5):679–687. https://www.ncbi.nlm.nih.gov/pubmed/24403609, doi: 10.1091/mbc.E13-10-0618.

Berro J, Pollard TD. Local and global analysis of endocytic patch dynamics in fission yeast using a new "temporal superresolution" realignment method. Molecular Biology of the Cell. 2014; 25(22):3501–3514. https://doi.org/10.1091/mbc.e13-01-0004, doi: 10.1091/mbc.e13-01-0004, pMID: 25143395.

Berro J, Sirotkin V, Pollard TD. Mathematical Modeling of Endocytic Actin Patch Kinetics in Fission Yeast: Disassembly Requires Release of Actin Filament Fragments. Molecular Biology of the Cell. 2010; 21(16):2905–2915. https://doi.org/10.1091/mbc.e10-06-0494, doi: 10.1091/mbc.e10-06-0494, pMID: 20587776.

Boulant S, Kural C, Zeeh JC, Ubelmann F, Kirchhausen T. Actin dynamics counteract membrane tension during clathrin-mediated endocytosis. Nature Cell Biology. 2011; 13(9):1124–1131. https://doi.org/10.1038/ncb2307, doi: 10.1038/ncb2307.

Carlsson AE. Membrane bending by actin polymerization. Current Opinion in Cell Biology. 2018; 50:1 – 7. http://www.sciencedirect.com/science/article/pii/S095506741730128X, doi: https://doi.org/10.1016/j.ceb.2017.11.007, cell Architecture.

Carlsson AE, Bayly PV. Force Generation by Endocytic Actin Patches in Budding Yeast. Biophysical Journal. 2014; 106(8):1596 – 1606. http://www.sciencedirect.com/science/article/pii/S0006349514002823, doi: https://doi.org/10.1016/j.bpj.2014.02.035.

Cuvelier D, Derényi I, Bassereau P, Nassoy P. Coalescence of Membrane Tethers: Experiments, Theory, and Applications. Biophysical Journal. 2005; 88(4):2714 – 2726. http://www.sciencedirect.com/science/article/pii/S0006349505733257, doi: https://doi.org/10.1529/biophysj.104.056473.

Dannhauser PN, Ungewickell EJ. Reconstitution of clathrin-coated bud and vesicle formation with minimal components. Nature Cell Biology. 2012; 14(6):634–639. https://doi.org/10.1038/ncb2478, doi: 10.1038/ncb2478.

Derényi I, Jülicher F, Prost J. Formation and Interaction of Membrane Tubes. Phys Rev Lett. 2002 May; 88:238101. http://link.aps.org/doi/10.1103/PhysRevLett.88.238101, doi: 10.1103/PhysRevLett.88.238101.

Dimova R, Aranda S, Bezlyepkina N, Nikolov V, Riske KA, Lipowsky R. A practical guide to giant vesicles. Probing the membrane nanoregime via optical microscopy. Journal of Physics: Condensed Matter. 2006; 18(28):S1151. http://stacks.iop.org/0953-8984/18/i=28/a=S04.

Dmitrieff S, Nédélec F. Membrane Mechanics of Endocytosis in Cells with Turgor. PLoS Comput Biol. 2015 10; 11(10):1–15. http://dx.doi.org/10.1371%2Fjournal.pcbi.1004538, doi: 10.1371/journal.pcbi.1004538.

Engqvist-Goldstein ÅEY, Drubin DG. Actin Assembly and Endocytosis: From Yeast to Mammals. Annual Review of Cell and Developmental Biology. 2003; 19(1):287–332. https://doi.org/10.1146/annurev.cellbio.19.111401.093127, doi: 10.1146/annurev.cellbio.19.111401.093127, pMID: 14570572.

Footer MJ, Kerssemakers JWJ, Theriot JA, Dogterom M. Direct measurement of force generation by actin filament polymerization using an optical trap. Proceedings of the National Academy of Sciences. 2007; 104(7):2181–2186. https://www.pnas.org/content/104/7/2181, doi: 10.1073/pnas.0607052104.

Fotin A, Cheng Y, Sliz P, Grigorieff N, Harrison SC, Kirchhausen T, Walz T. Molecular model for a complete clathrin lattice from electron cryomicroscopy. Nature. 2004 10; 432:573 EP –. https://doi.org/10.1038/nature03079.

Gallop JL, Jao CC, Kent HM, Butler PJG, Evans PR, Langen R, McMahon HT. Mechanism of endophilin N-BAR domain-mediated membrane curvature. The EMBO Journal. 2006; 25(12):2898–2910. https://www.embopress.org/doi/abs/10.1038/sj.emboj.7601174, doi: 10.1038/sj.emboj.7601174.

Goode BL, Eskin JA, Wendland B. Actin and endocytosis in budding yeast. Genetics. 2015; 199(2):315–358.

Hassinger JE, Oster G, Drubin DG, Rangamani P. Design principles for robust vesiculation in clathrin-mediated endocytosis. Proceedings of the National Academy of Sciences. 2017; 114(7):E1118–E1127. http://www.pnas.org/content/114/7/E1118, doi: 10.1073/pnas.1617705114.

Helfrich W. Elastic properties of lipid bilayers: theory and possible experiments. Zeitschrift für Naturforschung C. 1973; 28(11-12):693–703.

Henne WM, Kent HM, Ford MGJ, Hegde BG, Daumke O, Butler PJG, Mittal R, Langen R, Evans PR, McMahon HT. Structure and Analysis of FCHo2 F-BAR Domain: A Dimerizing and Membrane Recruitment Module that Effects Membrane Curvature. Structure. 2007 2020/05/13; 15(7):839–852. https://doi.org/10.1016/j.str.2007.05.002, doi: 10.1016/j.str.2007.05.002.

Jin AJ, Prasad K, Smith PD, Lafer EM, Nossal R. Measuring the Elasticity of Clathrin-Coated Vesicles via Atomic Force Microscopy. Biophysical Journal. 2006; 90(9):3333 – 3344. http://www.sciencedirect.com/science/article/pii/S0006349506725152, doi: https://doi.org/10.1529/biophysj.105.068742.

Jülicher F, Seifert U. Shape equations for axisymmetric vesicles: A clarification. Phys Rev E. 1994 May; 49:4728–4731. https://link.aps.org/doi/10.1103/PhysRevE.49.4728, doi: 10.1103/PhysRevE.49.4728.

Kaksonen M, Roux A. Mechanisms of clathrin-mediated endocytosis. Nature Reviews Molecular Cell Biology. 2018 02; 19:313 EP –. https://doi.org/10.1038/nrm.2017.132.

Kaksonen M, Toret CP, Drubin DG. Harnessing actin dynamics for clathrin-mediated endocytosis. Nature Reviews Molecular Cell Biology. 2006; 7(6):404–414. https://doi.org/10.1038/nrm1940, doi: 10.1038/nrm1940.

Kirchhausen T, Harrison SC. Protein organization in clathrin trimers. Cell. 1981; 23(3):755 – 761. http://www.sciencedirect.com/science/article/pii/0092867481904396, doi: https://doi.org/10.1016/0092-8674(81)90439-6.

Koster G, Cacciuto A, Derényi I, Frenkel D, Dogterom M. Force Barriers for Membrane Tube Formation. Phys Rev Lett. 2005 Feb; 94:068101. https://link.aps.org/doi/10.1103/PhysRevLett.94.068101, doi: 10.1103/PhysRevLett.94.068101.

Kübler E, Riezman H. Actin and fimbrin are required for the internalization step of endocytosis in yeast. The EMBO journal. 1993; 12(7):2855–2862.

Kukulski W, Schorb M, Kaksonen M, Briggs JAG. Plasma Membrane Reshaping during Endocytosis Is Revealed by Time-Resolved Electron Tomography. Cell. 2012; 150(3):508 – 520. http://www.sciencedirect.com/science/article/pii/S0092867412007842, doi: https://doi.org/10.1016/j.cell.2012.05.046.

Lacy MM, Ma R, Ravindra NG, Berro J. Molecular mechanisms of force production in clathrin-mediated endocytosis. FEBS Letters. 2018; 0(0). https://febs.onlinelibrary.wiley.com/doi/abs/10.1002/1873-3468.13192, doi: 10.1002/1873-3468.13192.

Lherbette M, RedlingshÃ¶fer L, Brodsky FM, Schaap IAT, Dannhauser PN. The AP2 adaptor enhances clathrin coat stiffness. The FEBS Journal. 2019; 286(20):4074–4085. https://febs.onlinelibrary.wiley.com/doi/abs/10.1111/febs.14961, doi: 10.1111/febs.14961.

Low PS, Chandra S. Endocytosis in plants. Annual review of plant biology. 1994; 45(1):609–631.

Lu R, Drubin DG, Sun Y. Clathrin-mediated endocytosis in budding yeast at a glance. Journal of Cell Science. 2016; 129(8):1531–1536. https://jcs.biologists.org/content/129/8/1531, doi: 10.1242/jcs.182303.

Ma R, Berro J. Structural organization and energy storage in crosslinked actin assemblies. PLOS Computational Biology. 2018 05; 14(5):1–25. https://doi.org/10.1371/journal.pcbi.1006150, doi: 10.1371/journal.pcbi.1006150.

Ma R, Berro J. Crosslinking actin networks produces compressive force. Cytoskeleton. 2019; 76(5):346–354. https://onlinelibrary.wiley.com/doi/abs/10.1002/cm.21552, doi: 10.1002/cm.21552.

McMahon HT, Boucrot E. Molecular mechanism and physiological functions of clathrin-mediated endocytosis. Nature Reviews Molecular Cell Biology. 2011; 12(8):517–533. https://doi.org/10.1038/nrm3151, doi: 10.1038/nrm3151.

Mettlen M, Chen PH, Srinivasan S, Danuser G, Schmid SL. Regulation of Clathrin-Mediated Endocytosis. Annual Review of Biochemistry. 2018; 87(1):871–896. https://doi.org/10.1146/annurev-biochem-062917-012644, doi: 10.1146/annurev-biochem-062917-012644, pMID: 29661000.

Minc N, Boudaoud A, Chang F. Mechanical Forces of Fission Yeast Growth. Current Biology. 2009; 19(13):1096 – 1101. http://www.sciencedirect.com/science/article/pii/S0960982209011324, doi: https://doi.org/10.1016/j.cub.2009.05.031.

Mooren OL, Galletta BJ, Cooper JA. Roles for actin assembly in endocytosis. Annual review of biochemistry. 2012; 81:661–686.

Mund M, van der Beek JA, Deschamps J, Dmitrieff S, Hoess P, Monster JL, Picco A, Nédélec F, Kaksonen M, Ries J. Systematic Nanoscale Analysis of Endocytosis Links Efficient Vesicle Formation to Patterned Actin Nucleation. Cell. 2018; 174(4):884 – 896.e17. http://www.sciencedirect.com/science/article/pii/S0092867418308006, doi: https://doi.org/10.1016/j.cell.2018.06.032.

Sirotkin V, Berro J, Macmillan K, Zhao L, Pollard TD, Schmid SL. Quantitative Analysis of the Mechanism of Endocytic Actin Patch Assembly and Disassembly in Fission Yeast. Molecular Biology of the Cell. 2010; 21(16):2894–2904. https://doi.org/10.1091/mbc.e10-02-0157, doi: 10.1091/mbc.e10-02-0157, pMID: 20587778.

Sorkin A, Puthenveedu MA. In: Yarden Y, Tarcic G, editors. Clathrin-Mediated Endocytosis New York, NY: Springer New York; 2013. p. 1–31. https://doi.org/10.1007/978-1-4614-6528-7_1, doi: 10.1007/978-1-4614-6528-7_1.

Sun Y, Martin AC, Drubin DG. Endocytic Internalization in Budding Yeast Requires Coordinated Actin Nucleation and Myosin Motor Activity. Developmental Cell. 2006; 11(1):33 – 46. http://www.sciencedirect.com/science/article/pii/S1534580706002462, doi: https://doi.org/10.1016/j.devcel.2006.05.008.

Tweten DJ, Bayly PV, Carlsson AE. Actin growth profile in clathrin-mediated endocytosis. Phys Rev E. 2017 May; 95:052414. https://link.aps.org/doi/10.1103/PhysRevE.95.052414, doi: 10.1103/PhysRevE.95.052414.

Walani N, Torres J, Agrawal A. Endocytic proteins drive vesicle growth via instability in high membrane tension environment. Proceedings of the National Academy of Sciences. 2015; 112(12):E1423–E1432. http://www.pnas.org/content/112/12/E1423, doi: 10.1073/pnas.1418491112.

Wang X, Galletta BJ, Cooper JA, Carlsson AE. Actin-Regulator Feedback Interactions during Endocytosis. Biophysical Journal. 2016; 110(6):1430 – 1443. http://www.sciencedirect.com/science/article/pii/S0006349516001648, doi: https://doi.org/10.1016/j.bpj.2016.02.018.

Wu XS, Elias S, Liu H, Heureaux J, Wen PJ, Liu AP, Kozlov MM, Wu LG. Membrane Tension Inhibits Rapid and Slow Endocytosis in Secretory Cells. Biophysical Journal. 2017; 113(11):2406 – 2414. http://www.sciencedirect.com/science/article/pii/S0006349517310810, doi: https://doi.org/10.1016/j.bpj.2017.09.035.

Yarar D, Waterman-Storer CM, Schmid SL. A Dynamic Actin Cytoskeleton Functions at Multiple Stages of Clathrin-mediated Endocytosis. Molecular Biology of the Cell. 2005; 16(2):964–975. https://doi.org/10.1091/mbc.e04-09-0774, doi: 10.1091/mbc.e04-09-0774, pMID: 15601897.

Appendix 1

Derivation of the analytical solution for the initiation force

The derivation here is based on the analytical solution obtained in the work of ***Derényi et al.*** (***2002***) in the limit of small angles. It assumes that the membrane is almost flat such that the tangential $\psi \ll 1$. Keeping only the first order of ψ and its derivatives and performing the coordinate transformation of $\psi(s)$ to $\psi(R)$, the shape equation can be reduced to

$$R^2\psi'' + R\psi' - (R^2\frac{\sigma_{\rm eff}}{\kappa} + 1)\psi = -\frac{f}{2\pi\kappa}R + \frac{p}{2\kappa}R^3 \tag{14}$$

where the prime (′) indicates the derivative with respect to the radial coordinate R and $\sigma_{\rm eff} = \sigma + \frac{1}{2}\kappa c_0^2$.

The general solution to ***Equation 14*** that satisfies the boundary condition at the tip $\psi(R = 0) = 0$ reads

$$\psi(R) = \frac{f}{2\pi\sigma_{\rm eff}}\frac{1}{R} - \frac{1}{2}\frac{p}{\sigma_{\rm eff}}R - \frac{f}{2\pi\sqrt{\kappa\sigma_{\rm eff}}}K_1(R\sqrt{\sigma_{\rm eff}/\kappa}) + cI_1(R\sqrt{\sigma_{\rm eff}/\kappa}) \tag{15}$$

where $I_i(x)$ and $K_i(x)$ are modified Bessel functions. The constant c is determined by the other boundary condition at $R = R_{\rm b}$. For the free-hinge BC, it reads

$$\psi' + \frac{\psi}{R} = c_0. \tag{16}$$

For fixed-hinge BC, it reads

$$\psi = 0. \tag{17}$$

To calculate the initiation force $F_{\rm init}$, we set the membrane height $L = 0$, i.e.,

$$\int_0^{R_{\rm b}} \psi(R) = 0 \tag{18}$$

For the free-hinge BC, the initiation force in the limit of $\sigma \to 0$ reads

$$\frac{F_{\rm init}}{2\pi} = \frac{4(\kappa c_0^3 + 2p)\left[1 - I_0(c_0R_{\rm b}/\sqrt{2})\right] + pc_0^2R_{\rm b}^2I_0(c_0R_{\rm b}/\sqrt{2})}{2c_0^2\left\{2K_0(c_0R_{\rm b}/\sqrt{2}) + I_0(c_0R_{\rm b}/\sqrt{2})\left[2\gamma - \ln(8) + 2\ln(c_0R_{\rm b})\right]\right\}}, \tag{19}$$

where γ is the Euler constant. As a special case $c_0 \to 0$, Eq. (19) reduces to

$$F_{\rm init} = \frac{3}{8}\pi R_{\rm b}^2 p \tag{20}$$

For the fixed-hinge BC, the initiation force reads

$$\frac{F_{\rm init}}{2\pi} = pR_{\rm b}^2\frac{4 - 4I_0(Q) + 2QI_1(Q)}{16 - 8I_0(Q) - 8QK_1(Q) + 4QI_1(Q)(2\ln Q - \ln 4 + 2\gamma)}, \tag{21}$$

where $Q = c_0R_{\rm b}/\sqrt{2}$. As a special case $c_0 \to 0$, Eq. (21) reduces to

$$F_{\rm init} = \frac{1}{4}\pi R_{\rm b}^2 p \tag{22}$$

Appendix 2

Spherical cap approximation

We approximate the dome-shaped membrane with a spherical cap of radius R (see ***Figure 7***a and b, inset). The shape of the spherical cap is fully determined by two parameters, the sphere radius R and the base radius R_b. Note that neither the free-hinge BC nor the fixed-hinge BC is satisfied in this case. The membrane height L of the spherical cap reads

$$L = R - \sqrt{R^2 - R_b^2}, \tag{23}$$

and the corresponding membrane area $A = 2\pi RL$ and the volume $V = \frac{1}{3}\pi L^2(3R - L)$. The free energy of the membrane then becomes

$$E = \left[\frac{1}{2}\kappa(\frac{2}{R} - c_0)^2 + \sigma\right] A + pV. \tag{24}$$

In the case of a fixed base radius, the free energy $E(R; c_0, R_b)$ is a function of only R. For a barely coated membrane, i.e., $c_0 R_p = 0$, the free energy $E(R; c_0, R_b)$ decreases monotonically with the radius R and the flat shape ($R = \infty$) has the lowest energy (***Figure 7***a). However, when c_0 becomes large, e.g., $c_0 R_p = 1$, the free energy $E(R; c_0, R_b)$ has a minimum at a finite radius R (***Figure 7***b). This means the flat shape is no longer stable and the membrane can be bent up by proteins without any external forces.

If the base radius is free to move, i.e., R_b being a free parameter, the free energy $E(R, R_b; c_0)$ becomes a function of both R and R_b, and always has its trivial minimum $E = 0$ at $R_b = 0$, regardless of the spontaneous curvature c_0 (***Figure 7***a and b, $R_b = 0R_p$). The corresponding solution at $R_b = 0$ represents an infinitely small patch of membrane. In the presence of an external force f, the total free energy $F(R, R_b; c0, f) = E(R, R_b; c0, f) - fL$ can have a nontrivial minimum with a nonzero R_b. The minimum force $f_{\min}$ to have such a nontrivial minimum, i.e., to lift the membrane up, is given by

$$f_{\min} = \min_{R, R_b} \frac{E}{L}. \tag{25}$$

Both the denominator and the numerator are positive numbers, therefore $f_{\min}$ is always positive. For instance, for $c_0 R_p = 1$, the minimum force $f_{\min} = 0.0027 f_p$ is obtained at $R = 1.998 R_p$ and $R_b = 0.00057 R_p$. Therefore an external force is always required to lift the membrane up in this condition. However, the base radius $R_b = 0.00057 R_p$ is an unrealistically narrow shape given the typical value of $R_p = 15\text{-}30\ \mathrm{nm}$. Similar problem also exists in the model of ***Dmitrieff and Nédélec*** (***2015***) which used a freely-moving base BC.

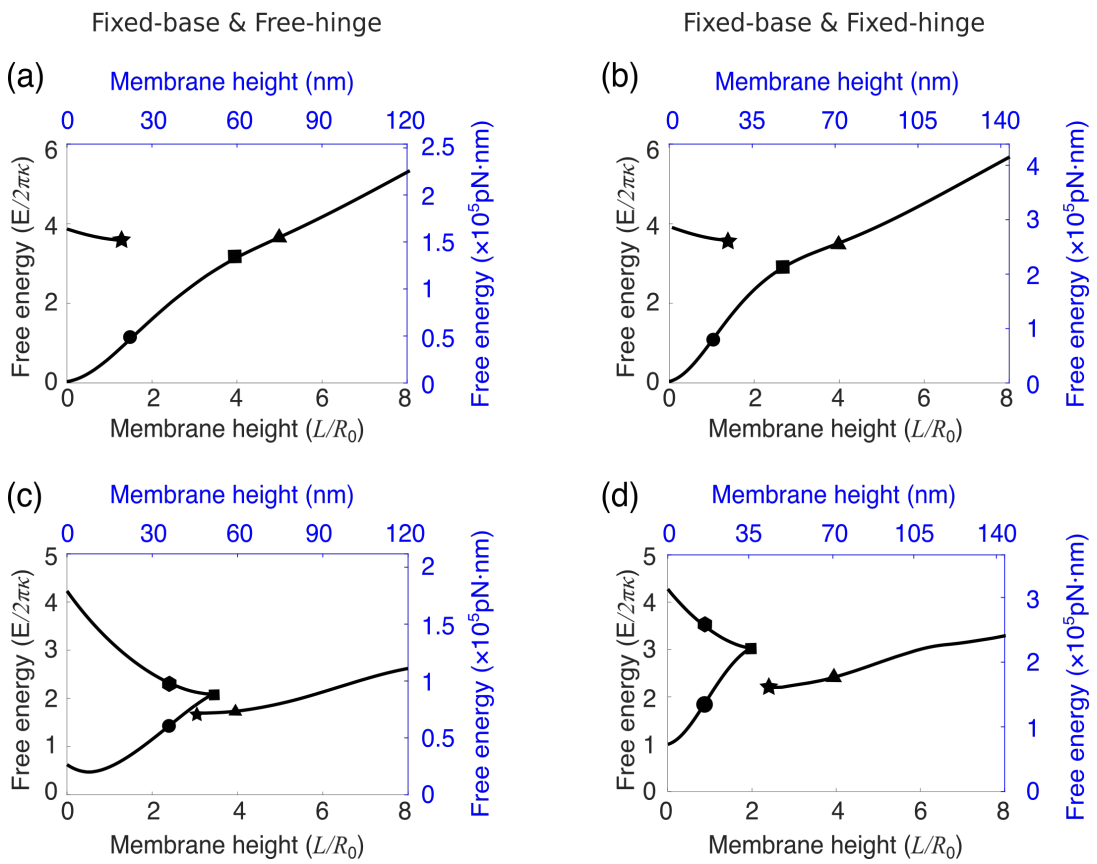

Figure 3–Figure supplement 1. (a-d) Free energy of membrane deformations E as a function of membrane height L. The spontaneous curvature is fixed at $c_0 R_\mathrm{p} = 0.2$ in (a, b) and $c_0 R_\mathrm{p} = 1$ in (c, d). The symbols on the E-L curve correspond to the same symbols on the f-L curve shown in Figure 3a-d. In the left column (a, c), the free-hinge BC is imposed at the base points $R_\mathrm{b} = 2R_\mathrm{p}$, while in the right column (b, d), the fixed-hinge BC is imposed. On the left and bottom axes (black), non-dimensionalized quantities are used, while on the right and top axes (blue), quantities are measured in their physical units. The parameters are listed in Table 2.

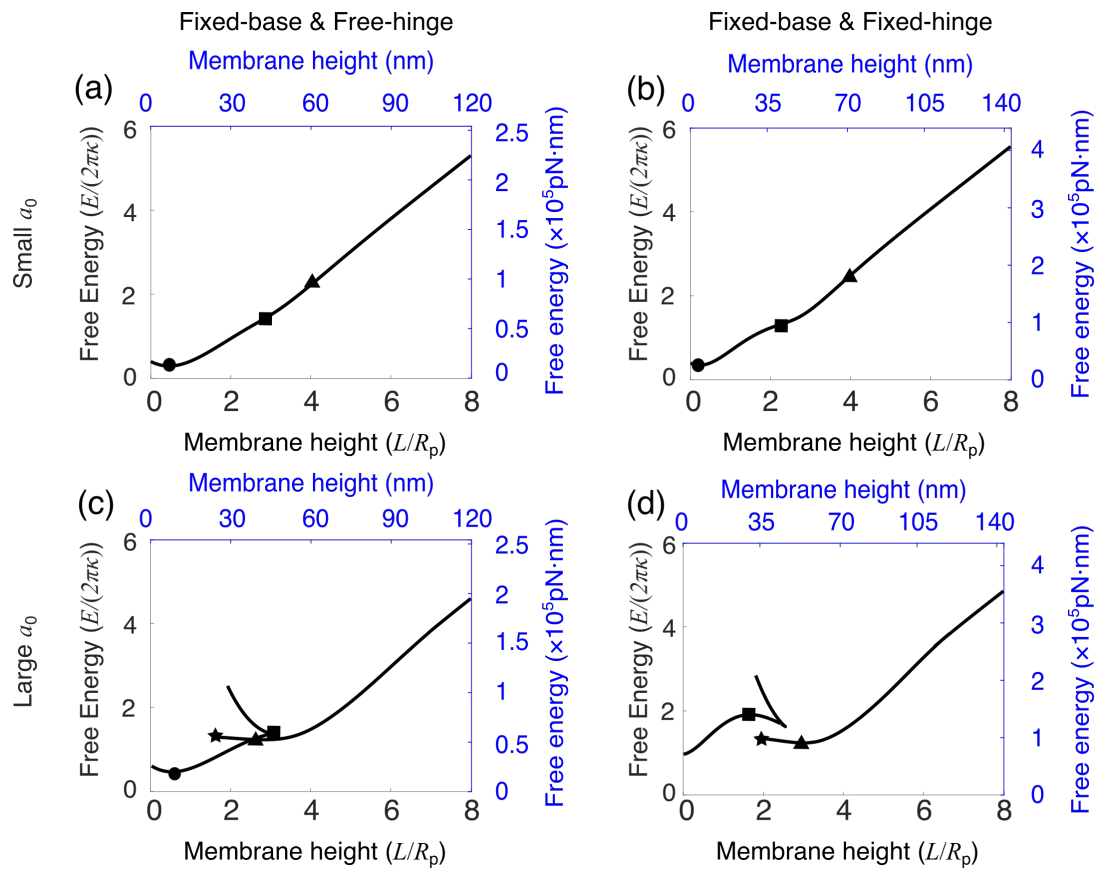

Figure 4–Figure supplement 1. (a - d) Free energy of membrane deformations E as a function of membrane height L. The coating area is fixed at $a_0/(2\pi R_p^2) = 1$ in (a, b) and $a_0/(2\pi R_p^2) = 2$ in (c, d). The symbols on the E-L curve correspond to the same symbols on the f-L curve shown in **Figure 4**a-d. In the left column (a, c), the free-hinge BC is imposed at the base points $R_b = 2R_p$, while in the right column (b, d), the fixed-hinge BC is imposed. On the left and bottom axes (black), non-dimensionalized quantities are used, while on the right and top axes (blue), quantities are measured in their physical units. The parameters are listed in **Table 2**.

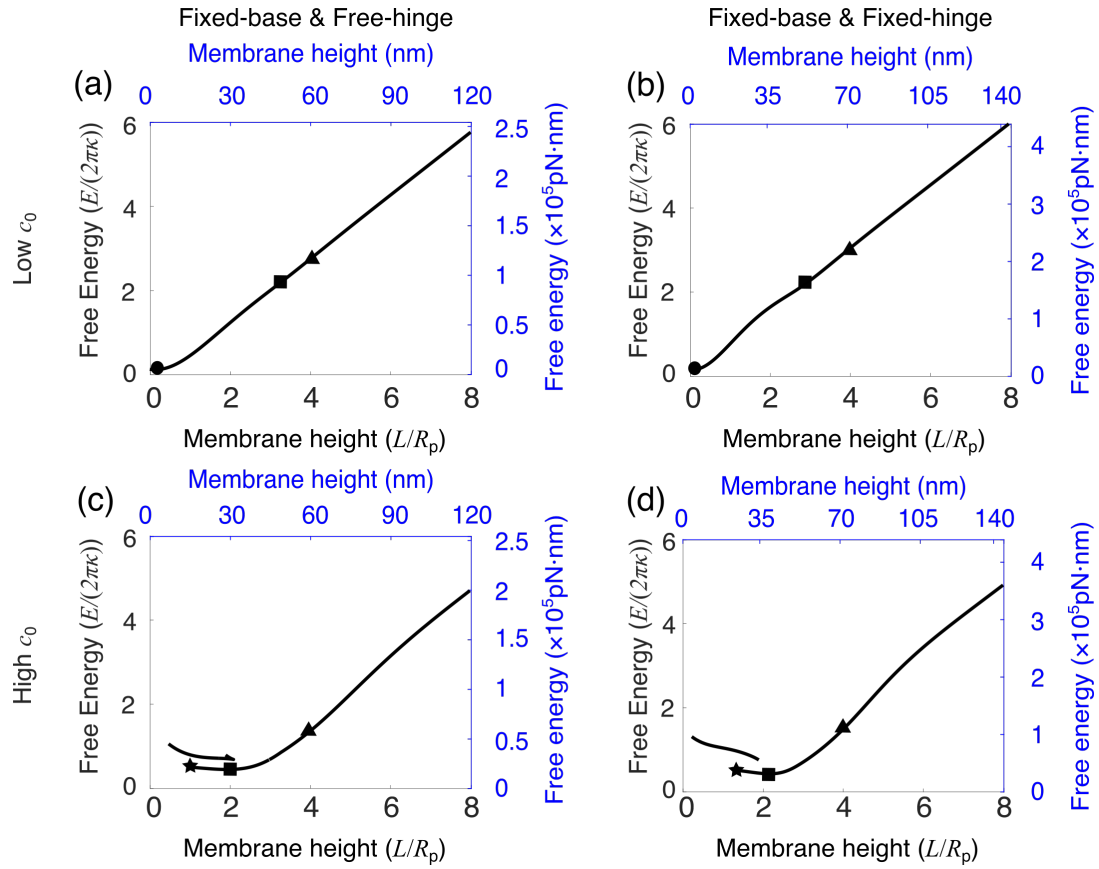

Figure 5–Figure supplement 1. (a - d) Free energy of membrane deformations E as a function of membrane height L. The coating area is fixed at $a_0/(2\pi R_p^2) = 1$ in (a, b) and $a_0/(2\pi R_p^2) = 2$ in (c, d). The symbols on the E-L curve correspond to the same symbols on the f-L curve shown in Figure 4a-d. In the left column (a, c), the free-hinge BC is imposed at the base points $R_b = 2R_p$, while in the right column (b, d), the fixed-hinge BC is imposed. On the left and bottom axes (black), non-dimensionalized quantities are used, while on the right and top axes (blue), quantities are measured in their physical units. The parameters are listed in Table 2.

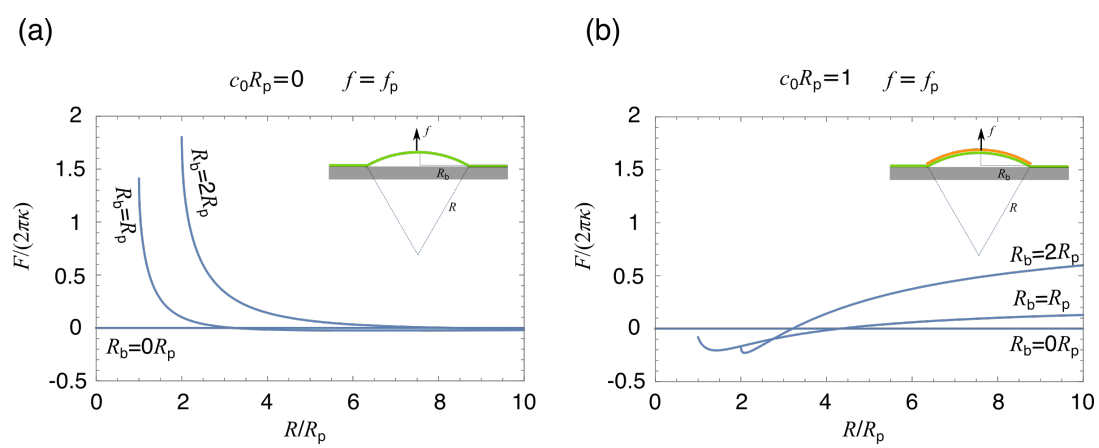

Figure 7–Figure supplement 1. Free energy of the membrane as a function of the sphere radius R for $c_0R_p = 0$ in (a) and $c_0R_p = 1$ in (b). The external force $f = f_p$. For different base radii R_b, the range of R is $[R_b, \infty]$, where $R = R_b$ corresponds to a hemi-spherical cap and $R = \infty$ corresponds to a flat shape.